Mineralium Deposita (2025) 60:551–580
https://doi.org/10.1007/s00126-024-01288-x

ARTICLE

Magnetite geochemistry as a proxy for metallogenic processes: A study on sulfide-mineralized mafic–ultramafic intrusions peripheral to the Kunene Complex in Angola and Namibia

Lorenzo Milani[1] · Lize Oosthuizen[1] · Trishya M. Owen-Smith[2] · Grant M. Bybee[3] · Ben Hayes[3] · Jérémie Lehmann[2] · Hielke A. Jelsma[4]

Received: 16 January 2024 / Accepted: 29 May 2024 / Published online: 19 June 2024

Abstract

Trace element concentrations in magnetite are dictated by the petrogenetic environment and by the physico-chemical conditions during magmatic, hydrothermal, or sedimentary processes. This makes magnetite chemistry a useful tool in the exploration of ore-forming processes. We describe magnetite compositions from Ni-Cu-(PGE)-sulfide mineralized rocks from seven mafic–ultramafic intrusions peripheral to the Mesoproterozoic AMCG (anorthosite-mangerite-charnockite-granite) suite of the Kunene Complex of Angola and Namibia to investigate metallogenic processes through the geochemical characterization of Fe-oxides, which were analyzed in-situ via Electron Probe Microanalysis (EPMA), and Laser Ablation-Inductively Coupled Plasma-Mass Spectrometry (LA-ICP-MS). We identified magmatic magnetite, segregated from both a silicate liquid and an immiscible sulfide liquid. Elements like Cr, Co and V suggest that the sulfide-related magnetite segregated from a relatively primitive Fe-rich monosulfide solid solution (MSS). Secondary Cr-rich magnetite appears in intrusions with abundant chromite or Cr-spinel. Two types of hydrothermal magnetite were identified, related to the pervasive replacement of sulfides and a late-stage, low-T fluid circulation event. Magnetite replacing sulfides is associated with serpentinized ultramafic rocks and is preferentially observed in the intrusions with the highest base and precious metal tenors. The high concentration of Ni, Co, Cu, Pd, As and Sb in these grains is corroborated by the identification of micron-size PGE mineral inclusions. We infer that serpentinization during hydrothermal fluid circulation was accompanied by desulphurization of sulfides with metal remobilization and reconcentration to generate magnetite carrying Pd microinclusions. We suggest that the highly serpentinized ultramafic rocks in the Kunene Complex region may become a possible target for economic Ni-Cu-(PGE) mineralization.

Keywords Magnetite · Kunene · Sulfide mineralization · AMCG complexes

Introduction

Magmatic nickel-copper-platinum group elements (Ni-Cu-PGE) deposits in mafic–ultramafic intrusions account for > 50% of the Ni and > 95% of the Pt and Pd currently produced (Mudd and Jowitt 2022). Many of the major magmatic Ni-Cu-PGE sulfide deposits, like Noril'sk (Russia), Voisey's Bay (Canada), and Jinchuan (China), are found in relatively small (a few square kilometres) mafic–ultramafic intrusive bodies (Lightfoot and Evans-Lamswood 2015; Barnes et al. 2016; Barnes 2023).

The typical phases that form from an immiscible sulfide liquid are pyrrhotite, pentlandite, chalcopyrite and pyrite (Naldrett 2004). However, the immiscible sulfide liquid may contain appreciable amounts of dissolved oxygen, resulting

Editorial handling: E. Mansur

✉ Lorenzo Milani
lorenzo.milani@up.ac.za

[1] Department of Geology, University of Pretoria, Private Bag X20, Hatfield 0028, South Africa

[2] Department of Geology, University of Johannesburg, Auckland Park 2006, P.O. Box 524, Johannesburg, South Africa

[3] School of Geosciences, University of the Witwatersrand, 1 Jan Smuts Avenue, Braamfontein 2000, Johannesburg, South Africa

[4] Anglo American Group Discovery and Geosciences, Johannesburg, South Africa

in the crystallization of primary magnetite, both in the early-stage Fe-rich monosulfide solid solution (MSS) and in the later, lower temperature, Cu-rich intermediate solid solution (ISS) (e.g., Dare et al. 2012). Primary magmatic magnetite can therefore form both via fractional crystallization of a silicate magma and a sulfide liquid (e.g., Duran et al. 2020). Furthermore, post-magmatic hydrothermal oxidation processes can affect the primary sulfide mineralization, and precipitate secondary, low-temperature magnetite (e.g., Evans 2008; Konnunaho et al. 2013; Nadoll et al. 2014; Yang et al. 2018; Beinlich et al. 2020).

Magnetite is one of the most abundant oxide minerals in the continental crust, easily preserved due to its resistance to weathering and erosion. It commonly contains trace elements that will partition differently according to parameters like temperature, oxygen fugacity, and magma/fluid composition (Dupuis and Beaudoin 2011; Dare et al. 2012). The properties of magnetite make this mineral a successful indicator in early-stage metal exploration, capable to constrain petrogenetic environments (Dupuis and Beaudoin 2011; Nadoll et al. 2014; Boutroy et al. 2014; Dare et al. 2014; Liu et al. 2015; Zhao and Zhou 2015; Duran et al. 2016a; Ward et al. 2018; Jiao et al. 2019; Moilanen et al. 2020), deposit types (Dupuis and Beaudoin 2011), and to discriminate between mineralized and barren rocks (Pisiak et al. 2017; Ward et al. 2018).

In this paper, we present results of magnetite geochemistry associated with mafic–ultramafic intrusions peripheral to the Mesoproterozoic Kunene AMCG (anorthosite-mangerite-charnockite-granite) Complex (KC) of Angola and Namibia. The KC, dated between 1.50 and 1.35 Ga, has an exposure exceeding 20,000 km^2, and is one of the largest known AMCG suites on Earth (Bybee et al. 2019, and references therein; Milani et al. 2022). On its western and southern margins, the KC is flanked by a series of relatively small (~ 10 km^2) mafic–ultramafic intrusions, which may be genetically related to the KC, and where previous exploration revealed the occasional presence of Ni-Cu-(PGE) mineralization (e.g., Maier et al. 2013).

The focus of this paper is not on the economic potential of individual intrusions, which would require a study of oxides of all the lithologies of each intrusion, but on the recognition of metallogenic processes through textural and geochemical characterization of Fe-oxides. Thin sections from seven mafic–ultramafic intrusions located near the KC were observed, and different magnetite types were identified according to size, shape, texture and mineral associations. Magnetite was analyzed via electron probe microanalysis (EPMA), and Laser Ablation-Inductively Coupled Plasma-Mass Spectrometry (LA-ICP-MS).

We distinguish magmatic and hydrothermal magnetite according to texture, phase relations and geochemistry. Primary magmatic magnetite is associated with silicate and sulfide liquids, with degree of sulfide liquid fractionation indicated by the oxide chemistry of primary magnetite. Secondary hydrothermal magnetite fingerprints post-crystallization processes, suggesting metal enrichment at a later stage. These findings have implications for the economic potential of mafic–ultramafic intrusions at the margins of the KC.

Geological setting

The Kunene Complex

The Mesoproterozoic Kunene AMCG Complex (KC) of southern Angola and northern Namibia (Fig. 1) is hosted by Paleoproterozoic basement rocks along the south-western part of the Angolan Shield of the Congo Craton of Central Africa (Jelsma et al. 2018). These supracrustal rocks have been recently divided, from north to south, in Central Eburnean Zone, Namibe Zone and Epupa Metamorphic Complex (Ferreira et al. 2024).

In Angola, the KC intruded a volcano-sedimentary sequence (de Carvalho and Alves 1993), and the Paleoproterozoic granitoids of the Regional Granite, dated at 2050–1780 Ma (Pereira et al. 2011; McCourt et al. 2013; Lehmann et al. 2020; Milani et al. 2022). The Regional Granite is unconformably overlain by the sedimentary succession of the Chela Group, forming the Humpata Plateau (Fig. 1), and dated at 1800–1500 Ma (Ernst et al. 2013; McCourt et al. 2013). The eastern margin of the KC in Angola is covered by Kalahari Group sediments, and recent gravimetric modelling attests to a possible AMCG extension of up to 42,500 km^2 (Rey-Moral et al. 2022).

The 1860–1730 Ma migmatites and orthogneisses of the Epupa Metamorphic Complex (Drüppel et al. 2007; Kröner et al. 2010, 2015) are the host rocks to the KC in northern Namibia, and were affected by pre-, syn-, and post-Kunene metamorphism (Seth et al. 2003, 2005; Brandt et al. 2021) (Fig. 1).

The KC mainly consists of large bodies of anorthosite sensu stricto, leucotroctolite, leuconorite and leucogabbronorite (Ashwal and Twist 1994; Drüppel et al. 2007; Bybee et al. 2019). In northern Namibia, the complex forms a broadly E-W-trending antiform known as the Zebra Lobe, composed of layers of olivine-bearing and pyroxene-bearing anorthositic rocks (Maier et al. 2013). The MCG component of the KC is mainly represented by the Red Granite Suite, an A-type granitoid consisting of granite porphyry, and minor mangerite, charnockite, granodiorite, syenite, and monzonite, in magmatic contact with the anorthosite suite (Milani et al. 2022).

Recent ID-TIMS U–Pb zircon and baddeleyite dates for the KC anorthosite suite in Angola are bracketed between 1440 and 1375 Ma, but evolved pegmatoidal mineralized

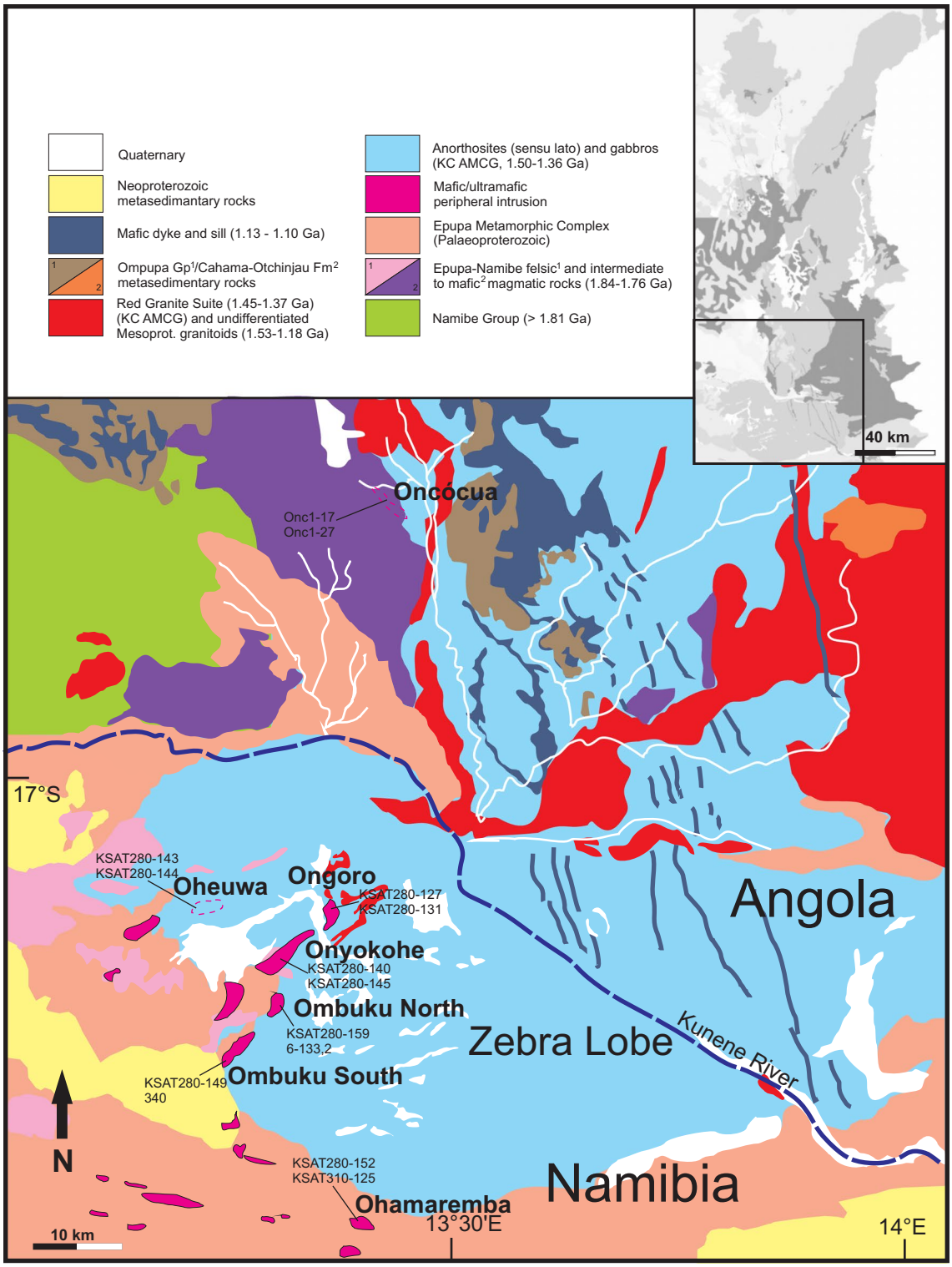

Fig. 1 The locations of the seven studied mineralized intrusions peripheral to the Kunene AMCG Complex in southern Angola and northern Namibia. The Oheuwa and Oncócua boundaries are inferred (purple dashed lines). The labels of the 14 thin sections object of the study are also reported. The inset shows the total extent of the exposed KC (after Ferreira et al. 2024)

pods in anorthosite yield an older age at ca. 1500 Ma (Bybee et al. 2019, and unpublished data). The age of the Red Granite Suite has been constrained between 1450 and 1360 Ma (Lehmann et al. 2020; Milani et al. 2022). In Namibia, there are few constraints on the age of the anorthosite suite, with only one U–Pb baddeleyite date of 1363 ± 17 Ma for the olivine-bearing anorthosite (Maier et al. 2013). The overall ages for the KC attest to a prolonged timescale of emplacement, possibly exceeding 140 Myr (Bybee et al. 2019; Milani et al. 2022).

The magmatism of the KC has been associated with a period of extensional tectonics during the breakup of the Columbia supercontinent (Mayer et al. 2004; Evans 2013). The timing of KC magmatism is similar to the 'Kibaran' magmatic event, 2100 km to the northeast (Tack et al. 2010) and has led to the suggestion that they are both related to a single Large Igneous Province (LIP) along the margins of the Congo Craton, with magmatism peaking at 1.38 Ga (Ernst et al. 2013; Mäkitie et al. 2014; Blanchard et al. 2017). However, magmatic and ductile deformational structures were observed by Lehmann et al. (2020) in KC anorthosite rocks, Red Granite and their basement rocks along the southwestern margin of the KC in Angola, with evidence of E–W contraction between 1400 and 1380 Ma. Together with other petrological, geochemical and geochronological evidence (Brower 2017; Bybee et al. 2019; Milani et al. 2022; Ferreira et al. 2024), a convergent continental margin during regional shortening is our preferred tectonic setting for the KC.

Mafic/ultramafic intrusions

Several small (< 10 km^2) mafic–ultramafic intrusions have been documented along the western and southern margins of the KC in Namibia and Angola, all located within 40 km of the anorthosite suite (Fig. 1; Simpson et al. 1970; Maier et al. 2008, 2013). They have been inferred to represent satellite bodies to the KC (Simpson et al. 1970). However, the age and genetic relations between these intrusions and the KC are still poorly constrained. Some of the intrusions are lithologically complex, ranging from dunite to harzburgite, troctolite, pyroxenite, gabbro, and anorthosite, whereas others are made up predominantly of a single lithology (Maier et al. 2008).

Preliminary exploration revealing copper and nickel mineralization was conducted in the 1970s on some of the peripheral mafic–ultramafic intrusions in Angola and in Namibia. The economic potential of mafic–ultramafic intrusions in association with Proterozoic massif-type anorthosites was boosted after the discovery in 1993 of the Voisey's Bay Ni-Cu-Co sulfide deposit in the Nain Plutonic Suite, Canada (Ryan et al. 1995; Naldrett 1997; Li and Naldrett 1999; Kerr and Smith 1997; Ryan 2000; Scoates and Mitchell 2000). Investigations and drilling in Namibia and Angola identified approximately 50 mafic–ultramafic peripheral intrusions (Maier et al. 2013, and references therein). At the moment, active exploration is ongoing both to the west and to the east of the KC, the latter covered by Kalahari sands.

This work is focused on the intrusions of Ohamaremba, Oheuwa, Ombuku North, Ombuku South, Ongoro and Onyokohe in Namibia, and Oncócua in Angola (Fig. 1). These intrusions commonly host Ni-Cu sulfides (chalcopyrite and pentlandite associated with predominant pyrrhotite). By combining petrography with high-resolution elemental analysis on Fe-oxides (magnetite and Cr-rich magnetite), we aim to constrain the degree of sulfide liquid fractionation and to identify petrogenetic indicators and vectors to Ni-Cu-PGE mineralization.

Lithostratigraphy of the studied intrusions

Ohamaremba

The Ohamaremba intrusion crops out as an elongated ESE–WNW body approximately 1–2 km south of the Zebra Lobe (Fig. 1) and is hosted by the migmatites of the Epupa Metamorphic Complex. It extends for about 10 km along strike, with a width not exceeding 400 m and an estimated thickness of at least 750 m (Maier et al. 2013). The lithologies are mainly troctolite with minor olivine gabbronorite and anorthosite (Maier et al. 2013). The contact with the host rocks is inferred to be tectonic, following a system of reverse and strike-slip faults broadly oriented WNW–ESE (Hornsey et al. 2009; Maier et al. 2013).

Ombuku North and Ombuku South

Ombuku North crops out as an elongated NNE–SSW body at the western margin of the Zebra Lobe, with a strike length of 1600 m, width of 550 m, and a thickness of 350–400 m (Fig. 1, Hornsey et al. 2009). To the east, Ombuku North is flanked by Kunene anorthosite and leucotroctolite. Migmatitic amphibolitic gneiss of the Epupa Metamorphic Complex crops out at the western side of Ombuku North (Maier et al. 2013). Ultramafic rocks are prevalent at Ombuku North as altered dunite (serpentinite), harzburgite and pyroxenite, with minor norite and websterite. Both olivine and pyroxene are commonly replaced by either serpentine (plus magnetite) or actinolite-anthophyllite-talc-chlorite aggregates.

Ombuku South is an elongated NE-SW body with a strike length of 6–8 km, a width of ~ 3.5 km, and a thickness of at least 600 m. Gravity measurements suggest it is connected to Ombuku North (Selfe 2009). To the southwest, Ombuku South is dominated by dunite and olivine harzburgite, with

minor orthopyroxenite and numerous lenses of banded chromitite that can be up to 2 m in thickness. The eastern side of the intrusion is more composite and mafic in composition, with gabbro, mottled anorthosite and troctolite (Maier et al. 2013). The host rocks are mainly banded amphibolite and amphibolite gneiss of the Epupa Metamorphic Complex (Maier et al. 2013), whereas to the southwest the intrusion is overlain by the Neoproterozoic metasedimentary rocks of the Nosib Group of the Damara Supergroup.

Onyokohe

The intrusion crops out as an elongated NE–SW body approximately 5 km north of Ombuku North (Fig. 1), with a strike length of ~ 6 km, a width of ~ 1 km, and a thickness of ~ 400 m. The contacts with the host rock are not exposed, but the intrusion boundaries are characterized by the presence of intense faulting and common cataclasite zones, and a system of crosscutting NE–SW- and NW–SE-striking faults. The predominant lithologies are norite, troctolite, harzburgite, olivine gabbronorite, and minor pyroxenite.

Oheuwa

Oheuwa represents an E–W-trending body approximately 20 km north-west of the Zebra Lobe. It has an estimated length of 5 km, a width of ~ 1 km, and a thickness of at least 400 m (Fig. 1). The intrusion comprises olivine pyroxenite, anorthosite, troctolite and dunite, with minor harzburgite and norite. According to unpublished mapping and reports, the intrusion is hosted mainly by Kunene anorthositic rocks, whereas, to the south, drill cores show that the host rocks are orthogneiss of the Epupa Metamorphic Complex.

Ongoro

The Ongoro intrusion follows a fault system and crops out as an elongated NW–SE-trending body on the northwestern margin of the Zebra Lobe. The body is surrounded by KC anorthosite and has a length of ~ 4 km, a width of ~ 1 km, and a thickness of less than 100 m (Fig. 1). At the surface, the lithologies are represented by olivine norite and troctolite to leucotroctolite. At depth, pyroxenite, anorthosite and norite rocks become predominant and are commonly mylonitized, with the development of intense chlorite and epidote alteration.

Oncócua

The intrusion is located in Angola on the western margin of the KC, approximately 45 km north of the Zebra Lobe (Fig. 1), at the contact between Paleoproterozoic schists and granitoids and the KC anorthosite suite. The intrusion is poorly exposed and was detected mainly through soil geochemistry and electromagnetic geophysics, which revealed a 7.5 km-long NW–SE-striking anomaly, with a thickness of 200 m. Drilling indicates that the Oncócua intrusion is predominantly made up of medium- to coarse-grained apatite-orthopyroxenite, with up to 30% apatite, commonly as macrocrysts. Phlogopite is also common. Minor anorthosite and norite have also been intersected (Maier et al. 2013).

Sampling and analytical techniques

The seven mafic–ultramafic intrusions are representative of Ni-Cu mineralized intrusions along the exposed margins of the KC. Rock samples were selected from mineralized intervals in the 65 available boreholes drilled in the period 1999–2014 and from surface samples collected between 2015 and 2021. Fourteen polished thin sections representative of the different associations and textures of magnetite (+ ilmenite) were examined through microscopy and scanning electron microscopy (SEM). Back-scattered electron (BSE) images and semi-quantitative analyses of the minerals are in Table 1. Details on the instrumental settings are in ESM 1. The full dataset of EPMA analyses is in ESM2. The measures used to monitor the quality of the data are in ESM 3, and a complete dataset of LA-ICP-MS analyses is in ESM 4.

Results

Petrography

Ohamaremba. Troctolite samples KSAT310-125 and KSAT280-152 (Fig. 2a, b) are characterized by an uneven distribution of cumulus olivine aggregates and tabular plagioclase, with olivine progressively altered to serpentine, which occurs in dark-brown oxide-rich microveinlets cross-cutting the olivine grains. Plagioclase is labradorite-bytownite in composition (based on the extinction angle of twin lamellae), and rare clinopyroxene oikocrysts have been observed. Sulfides, mainly disseminated, occur as anhedral associations with oxides, with dominant pyrrhotite and minor pentlandite and chalcopyrite (Fig. 3a, b, d, e). A secondary generation of sulfides includes chalcopyrite as fine-grained disseminations or in association with veined magnetite (Fig. 3e). Magnetite crystallized in interstitial spaces between cumulus olivine and plagioclase (sideronitic texture), as discrete grains, and as late-stage veinlets (Fig. 3a-e). Ilmenite is commonly intergrown with magnetite, or occurs as exsolutions (Fig. 3a, c, d, e).

Ombuku North. Serpentinite KSAT280-159 (Fig. 2c) is characterized by coarse pseudomorphs of serpentine after cumulus olivine, in places bordered by fine-grained

Table 1 Summary of the location and petrographic data for the samples analyzed in this study. Abbreviations: Amph = amphibole, Ap = apatite, Ccp = chalcopyrite, Chl = chlorite, Cpx = clinopyroxene, Cr-Sp = Chromium-spinel, Cub = cubanite, Ep = epidote, Ferritchr = ferritchromite, Ilm = ilmenite, Mt = magnetite, Ol = olivine, Opq = opaque, Opx = orthopyroxene, Pn = pentlandite, Pl = plagioclase, Po = pyrrhotite, Serp = serpentine, Sp = spinel

Sample	Provenance	Location	Depth (m)	Rock type	Magnetite modal (%)	Magnetite **type**	Magnetite Veinlets	Mineral phases (%)	Main Opaques
Ohamaremba									
KSAT310-125	Surface sample	17.46086°S 13.38966°E	-	Troctolite	15	3, 5	Yes	Pl (55), Ol (30), Opq (15)	Mt, Cr-Mt, Ferritchr, Ilm, Po
KSAT280-152	Drill core KNAD002	17.460039°S 13.388763°E	-339	Troctolite	20	1	Yes	Ol (40), Pl (35), Opq (25)	Mt, Ilm, Po, Ccp, Pn, Cub
Ombuku N									
6–133,2	Drill core KNBD006	17.247571°S 13.322646°E	-133	Troctolite	15	2, 5	Yes	Serp (70), Opq (15), Amph (5), Ol (10)	Mt, Ilm, Po, Ccp, Pn, Cub
KSAT280-159	Drill core KNBD003	17.248231°S 13.319490°E	-235	Serpentinite	10	4	Yes	Serp (70), Opq (30)	Mt, Ferritchr, Po, Ccp, Pn
Ombuku S									
KSAT340	Surface sample	17.286915°S 13.261229°E	-	Serpentinite	5	3	Yes	Serp (60), Opq (40)	Cr-Sp, Ferritchr, Ilm,
KSAT280-149	Drill core KNCD001	17.300829°S 13.253771°E	-550	Harzburgite	10	3	No	Serp (70), Opq (30)	Ferritchr, Po, Ccp
Onyokohe									
KSAT280-140	Drill core KNV004	17.119012°S 13.206603°E	-103	Harzburgite	20	4, 5	Yes	Serp (55), Opx (25), Opq (20)	Mt, Po
KSAT280-145	Drill core KNV006	17.179741°S 13.323239°E	-161	Norite	40	2	No	Serp (60), Opq (40)	Mt, Ilm, Sp, Po
Oheuwa									
KSAT280-143	Drill core KNV003	17.118408°S 13.209804°E	-57	Olivine norite	10	2	No	Pl (50), Opq (20), Ol (20), Opx (10)	Mt, Ilm, Po, Pn
KSAT280-144	Drill core KNV003	17.118408°S 13.209804°E	-231	Websterite	20	1	No	Opx (50), Opq (30), Cpx (10), Ol (10)	Mt, Sp, Ilm, Po, Ccp, Pn
Ongoro									
KSAT280-127	Drill core KNV008	17.148773°S 13.381791°E	-75	Pyroxenite	10	1	No	Opq (70), Opx (20), Ep (5), Chl (5)	Mt, Ilm, Po, Ccp
KSAT280-131	Drill core KNV008	17.148773°S 13.381791°E	-78	Pyroxenite	5	1	No		Mt, Ilm, Po, Ccp
Oncócua									
ONC1-17	Drill core ONC 1	16.713089°S 13.441456°E	-96	Apatite Orthopyroxenite	20	1	No	Opx (50), Ol (20), Opq (20), Ap (10)	Ilm, Po, Opn, Ccp, Cub
ONC1-27	Drill core ONC 1	16.713089°S 13.441456°E	-99	Apatite Orthopyroxenite	15	1	No		Mt, Ilm, Po, Ccp, Pn, Cub

pyroxene as coronitic rims, with rare discrete orthopyroxene grains almost completely replaced by actinolite-anthophyllite. Sulfides are present as discrete anhedral grains or stringers of pentlandite and chalcopyrite with minor pyrrhotite and are intensively replaced by magnetite (Fig. 2c, 3f, g). Chromium-spinel is common as subhedral grains in association with magnetite and sulfides (Fig. 3g). Troctolite 6–133,2 (Fig. 2d) shows an uneven distribution of cumulus olivine in plagioclase. Brown iddingsite alteration is present and typically bordered by spinel and kaersutite, and plagioclase is locally deformed with the development of kink bands (Fig. 2d). Opaque minerals are a minor component (5% vol.), with sulfides mainly as pyrite and pyrrhotite as small blebs and stringers. Fe-Ti-oxides form aggregates, with ilmenite co-crystallized with magnetite (Fig. 3h). Late-stage hydrothermal magnetite in veinlets is common.

Ombuku South. Harzburgite KSAT280-149 (Fig. 2e) is a medium-grained rock with olivine and pyroxene intensely altered to talc, with anthophyllite, actinolite and chlorite. Sulfides are as lenses and band-like segregations of pyrite within the talc groundmass. Disseminated pyrrhotite, with small inclusions or veinlets of chalcopyrite, is also present (Fig. 3i, j). Serpentinite 340 (Fig. 2f) shows large and highly serpentinized olivine clusters, and abundant oxides as massive lenses, as well as with a sideronitic texture. Cr-spinel is common, typically replaced by Cr-rich magnetite (Cr-magnetite and ferritchromite) in patches (Fig. 3i, j) or as rims (Fig. 3k). Ilmenite is minor and mostly present as euhedral to subhedral grains co-crystallized with magnetite (Fig. 3i, j).

Onyokohe. KSAT280-140 (Fig. 2g) is a harzburgite with idiomorphic cumulus olivine and coarse-grained orthopyroxene. Olivine crystals are largely replaced by serpentine and fractures are filled with iddingsite veinlets, whereas orthopyroxene is replaced by chlorite and actinolite. Plagioclase is intensively saussuritized. Norite KSAT280-145 (Fig. 2h) shows large clinopyroxene crystals, partially altered and rimmed by green actinolite and chlorite. Plagioclase is rare and is intensively saussuritized and rimmed by epidote. In both samples, pyrrhotite and pyrite are the main sulfides, occurring as fine disseminations and blebs as inclusions in magnetite (Fig. 3l), or as individual laths (pyrite). Only rare chalcopyrite has been observed. In KSAT280-140, the oxides occur as subhedral primary magnetite grains and secondary late-stage veinlets (Fig. 3l), whereas the norite sample (KSAT280-145) is characterized by large subhedral magnetite grains co-crystallized with ilmenite. Magnetite shows cloth microtexture and fine spinel exsolution (pleonaste). A few large spinel crystals are also present (Fig. 4a).

Oheuwa. KSAT280-143 is an olivine norite with cumulus orthopyroxene aggregates in plagioclase (Fig. 2i), kaersutite and partially serpentinized olivine. KSAT280-144 (Fig. 2j) is a medium-grained websterite with orthopyroxene glomerocrysts. Micron-scale parallel exsolution lamellae of Cr-magnetite in orthopyroxene are responsible for the brown tint. Subhedral olivine is mostly replaced by serpentine, with rare relicts. In both thin sections, sulfides are mainly pyrrhotite, with minor chalcopyrite and pentlandite. Magnetite ranges from euhedral to anhedral and is characterized by ilmenite trellis exsolution and spinel micro-inclusions (pleonaste, Fig. 4b). Discrete euhedral ilmenite grains are typically intergrown with magnetite, with grain boundaries commonly occurring as spinel-lined serrated margins (Fig. 4b-d).

Ongoro. The two pyroxenite samples (KAC280-127 and KAC280-131) represent coarse-grained, locally pegmatoidal, pyroxenite rocks that host most of the Ni-Cu mineralization in this intrusion. Both samples (Fig. 2k, l) are characterized by large (mm-size) orthopyroxene crystals altered to serpentine, with the development of thin marginal kaersutite, and surrounded by a corona of actinolite and chlorite. Sulfides are pyrrhotite-dominated, but stringers, disseminations and veinlets of chalcopyrite and pentlandite are common (Fig. 4e, f). Individual grains of euhedral magnetite, within or in contact with pyrrhotite, are typically associated with ilmenite (Fig. 4e, f), and can include disseminated pentlandite (Fig. 4f). Ilmenite is also commonly present as elongated laths exsolved in magnetite (Fig. 4e-g). Spinel microgranules line the serrated margins between magnetite and ilmenite (Fig. 4f).

Oncócua. The selected samples (Onc1-17 and Onc1-27) are characterized by large oikocrysts (2–5 mm) of orthopyroxene, euhedral to subhedral apatite, minor olivine (partly serpentinized), plus opaque minerals (Fig. 2m, n). Orthopyroxene shows oxide exsolution lamellae, whereas apatite is present as single mm-size crystals, or as large aggregates. Opaque minerals make up 25% of the phases. Sulfides are present as net-textured or blebs of pyrrhotite, with lesser chalcopyrite, cubanite, pyrite and pentlandite, and are associated with the oxides, consisting of large (up to mm-size) magnetite/ilmenite aggregate pairs interstitial to orthopyroxene (Fig. 4h-k), or as stockwork veinlets, representing both primary and late-stage products. Ilmenite is also common as exsolution in magnetite (Fig. 4i-k), and as discrete primary crystals.

Oxide chemistry by electron microprobe (EPMA)

A total of 223 spots on Fe-oxides were analyzed by EPMA. Although less precise than LA-ICP-MS, this technique allowed us to investigate grains only a few microns in size, such as microcrystals and micron-wide veinlets. Analyses obtained from a small beam size are also advantageous as they are closer to the real oxide composition, as mixed results due to exsolution or microinclusions can be avoided. The EPMA data were therefore used for the Fe-oxide classification. Most of the magnetite grains plot at the magnetite

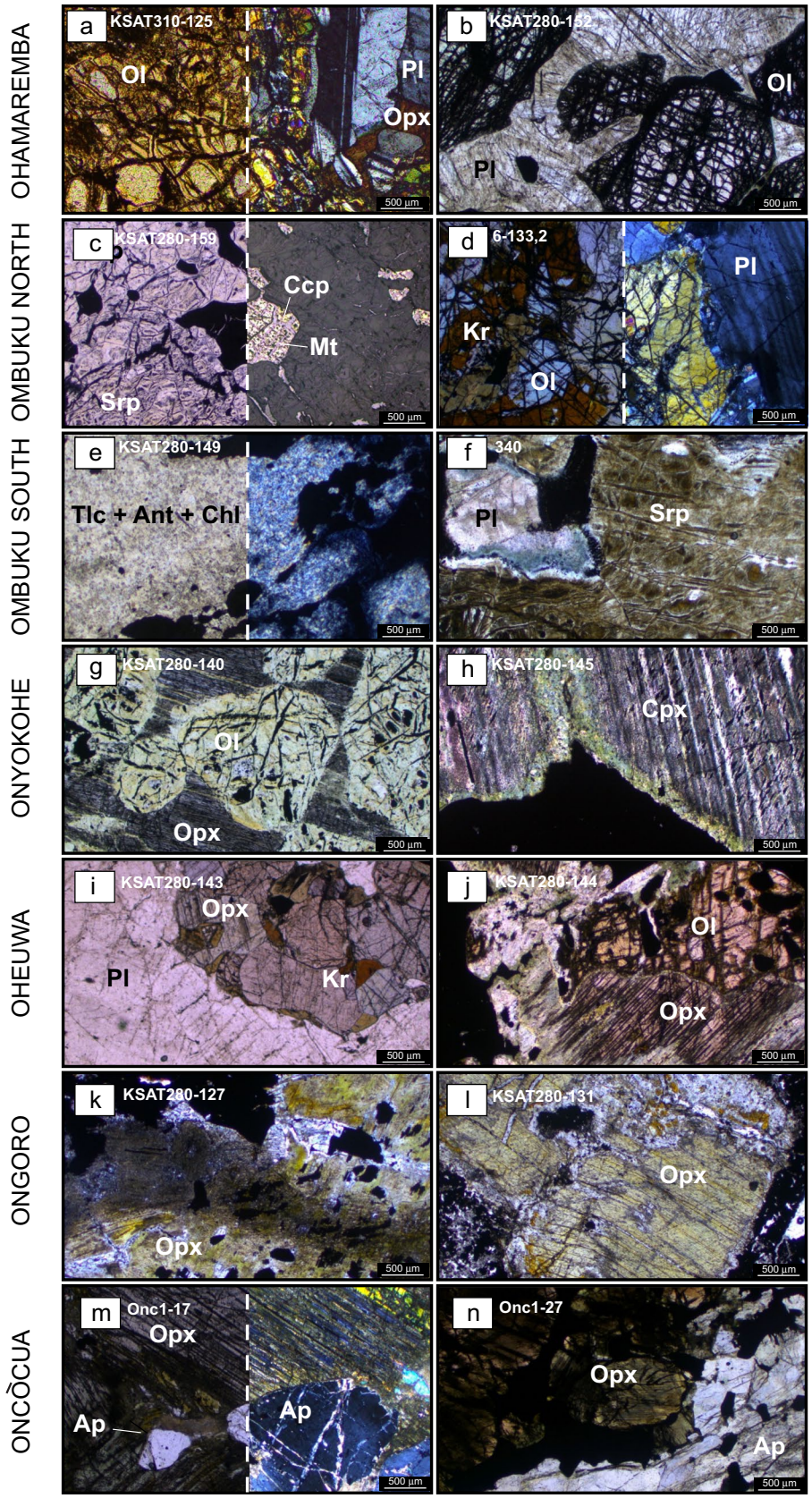
OHAMAREMBA
OMBUKU NORTH
OMBUKU SOUTH
ONYOKOHE
OHEUWA
ONGORO
ONCÕCUA
a KSAT310-125
Ol
Pl
Opx
b KSAT280-152
Ol
Pl
c KSAT280-159
Ccp
Mt
Srp
d 6-133,2
Pl
Kr
Ol
e KSAT280-149
Tlc + Ant + Chl
f 340
Pl
Srp
g KSAT280-140
Ol
Opx
h KSAT280-145
Cpx
i KSAT280-143
Opx
Pl
Kr
j KSAT280-144
Ol
Opx
k KSAT280-127
Opx
l KSAT280-131
Opx
m Onc1-17
Opx
Ap
Ap
n Onc1-27
Opx
Ap
500 µm

◂**Fig. 2** Transmitted and reflected light photomicrographs of the fourteen samples examined in this study (split plane- and cross-polarized transmitted light images in a, d, e, m, and split transmitted and reflected light images in c). **a**, **b**: Troctolite KSAT310-125 and KSAT280-152 showing large partially serpentinized cumulus olivine grains and laths of sausurritized plagioclase. **c**: Serpentinized dunite KSAT280-159 with chalcopyrite largely replaced by magnetite. **d**: Troctolite 6–133,2 with aggregates of cumulus olivine intersected by veinlets of iddingsite and rimmed by spinel and kaersutite. **e**: Harzburgite KSAT280-149 characterized by talc-altered mafic minerals. **f**: Dunite 340 intensely altered to phyllosilicates and chlorite with interstitial oxides. **g**: Idiomorphic and serpentinized cumulus olivine grains and interstitial orthopyroxene in harzburgite KSAT280-140. **h**: Large clinopyroxene rimmed by green actinolite and chlorite at the contact with massive oxide (magnetite/ilmenite) in norite KSAT280-145. **i**: Aggregates of cumulus orthopyroxene partially replaced by brown kaersutite and relatively unaltered plagioclase in olivine norite KSAT280-143. **j**: Orthopyroxene, serpentinized olivine, partially chloritized plagioclase and opaque minerals (mainly pyrrhotite and magnetite) in websterite KSAT280-144. **k**: Orthopyroxene altered to actinolite and chlorite characterise pyroxenite KSAT280-127. **L**: Large orthopyroxene grain partially altered to actinolite and brown kaersutite in pyroxenite KSAT280-131. **m**, **n**: Apatite-orthopyroxenites of Onc1-17 and Onc1-27 are characterized by large orthopyroxene oikocrysts and mm-size euhedral to subhedral apatite grains. Opaque minerals (sulfides and oxides) are mainly interstitial to orthopyroxene. Abbreviations: Ant = anthophyllite, Ccp = chalcopyrite; Chl = chlorite, Cpx = clinopyroxene, Kr = kaersutite, Mt = magnetite, Ol = olivine, Opx = orthopyroxene, Pl = plagioclase, Srp = serpentine, Tlc = talc

end of the magnetite-ulvöspinel solid solution line, with maximum TiO_2 at 21 wt% (Fig. 5a), with only a small number of analyses deviating towards the ulvöspinel endmember. The plot of the trivalent cations Al^{3+}, Cr^{3+}, and Fe^{3+} differentiates among the Cr-Fe-spinels (Fig. 5b), and the criteria proposed by Barnes and Roeder (2001) and Hodel et al. (2020) were adopted to define the compositional fields of magnetite sensu stricto (Cr_2O_3 0–6 wt%), Cr-magnetite (Cr_2O_3 6–13 wt%) and ferritchromite (Cr_2O_3 > 13 wt%). The complete dataset of analyses, including for spinel, is in ESM2, whereas Table 2 reports the average compositions of magnetite (including the microveinlets), Cr-magnetite and ferritchromite.

The EPMA data show notable variability among the seven intrusions, but also within each intrusion. Most of the data correspond to magnetite, typically as nearly pure Fe-oxide. Magnetite as thin veinlets is typically indistinguishable from discrete crystals (see troctolite KSAT310-125, harzburgite KSAT280-140 and websterite KSAT280-144 in ESM 2), suggesting that the two morphologies derive from the same crystallising fluid. The only microveinlets geochemically distinct from discrete magnetite grains are in troctolite KSAT280-152, where the stockwork of micron-wide veins is characterized by negligible Al, Cr and V. The relatively high Si and Mg (commonly > 1 wt%) in these veins is likely due to the incorporation of silicate phases during analysis. Magnetite at Oncócua (Onc1-27 and 1–27) shows the highest Ti (average 14,000 ppm), Al (9000 ppm), V (5000 ppm), and Zn (470 ppm). The presence of Cr in Cr-magnetite and ferritchromite is normally accompanied by relatively high Ti, Al, V, Mn, Ni and Zn. Cr-magnetite was recognized at Ohamaremba (troctolite KSAT310-125), where ferritchromite was also detected. Ferritchromite characterises most of the Fe-oxides analysed at Ombuku South, occurring as patches, single crystals or rims replacing large primary Cr-spinel oxides (Fig. 3k).

A comparison of the EPMA magnetite data between mafic and ultramafic rocks (4 and 8 samples, respectively) does not show any correlation with rock type or degree of fractionation, as spikes and depletions in element content seem randomly distributed and not driven by any geochemical signature of the whole rock.

Oxide chemistry by LA-ICP-MS

A total of 250 analyses were performed via LA-ICP-MS on magnetite, and on some Cr-magnetite and ferritchromite. The larger spot size than the EPMA implies that some analyses may have been affected by the incorporation of sulfide microinclusions. This explains the locally high chalcophile content in magnetite in some analyses at Ohamaremba (KSAT280-152) and Oncócua (Onc1-17) for Zn, and at Ombuku North (KSAT280-159) for Ni and Cu. The high Mg, Al and Mn recorded in other analyses suggest the incorporation of ilmenite or spinel during ablation, while the locally high silica may reflect the involvement of silicates. In order to reduce the impact of possible contaminants, 31 analyses with Si > 3 wt%, and/or Ni > 0.5 wt%, Cu > 0.3 wt% or Zn > 0.3 wt%, have been excluded from the discussion. A summary with the average compositions of the elements for each oxide type is shown in Table 3, while a full dataset, including analyses high in Ni, Cu, Zn, is in ESM 4.

The LA-ICP-MS data confirm a variable trace element content among, and within, the samples (see ESM 4). Magnetite from the Oheuwa olivine norite (KSAT280-143) shows the highest Cr, in the range 8000–27000 ppm, and is accompanied by high Ti (up to 40,000 ppm) and V (up to 8200 ppm). Low Cr, Ti and V (a few tens of ppm) are found in most of the magnetite of Ombuku North, Ohamaremba troctolite KSAT310-125, and Onyokohe harzburgite KSAT280-140. With the exception of serpentinite KSAT280-159 (Ombuku North), the low Cr, Ti and V are paired with relatively high Mg (mostly > 20,000 ppm). The chalcophile element contents (Mn, Ni, Co, Cu, Pb, Zn, Mo, Sn, As, Sb) can be affected by the incorporation of sulfide microinclusions. In the absence of sulfide microinclusions, we expect negligible chalcophile element contents in primary magnetite crystallized from a sulfide liquid, as such elements preferentially partition into the sulfide phase. In particular, high Ni, Zn and Cu were recorded in some analyses from

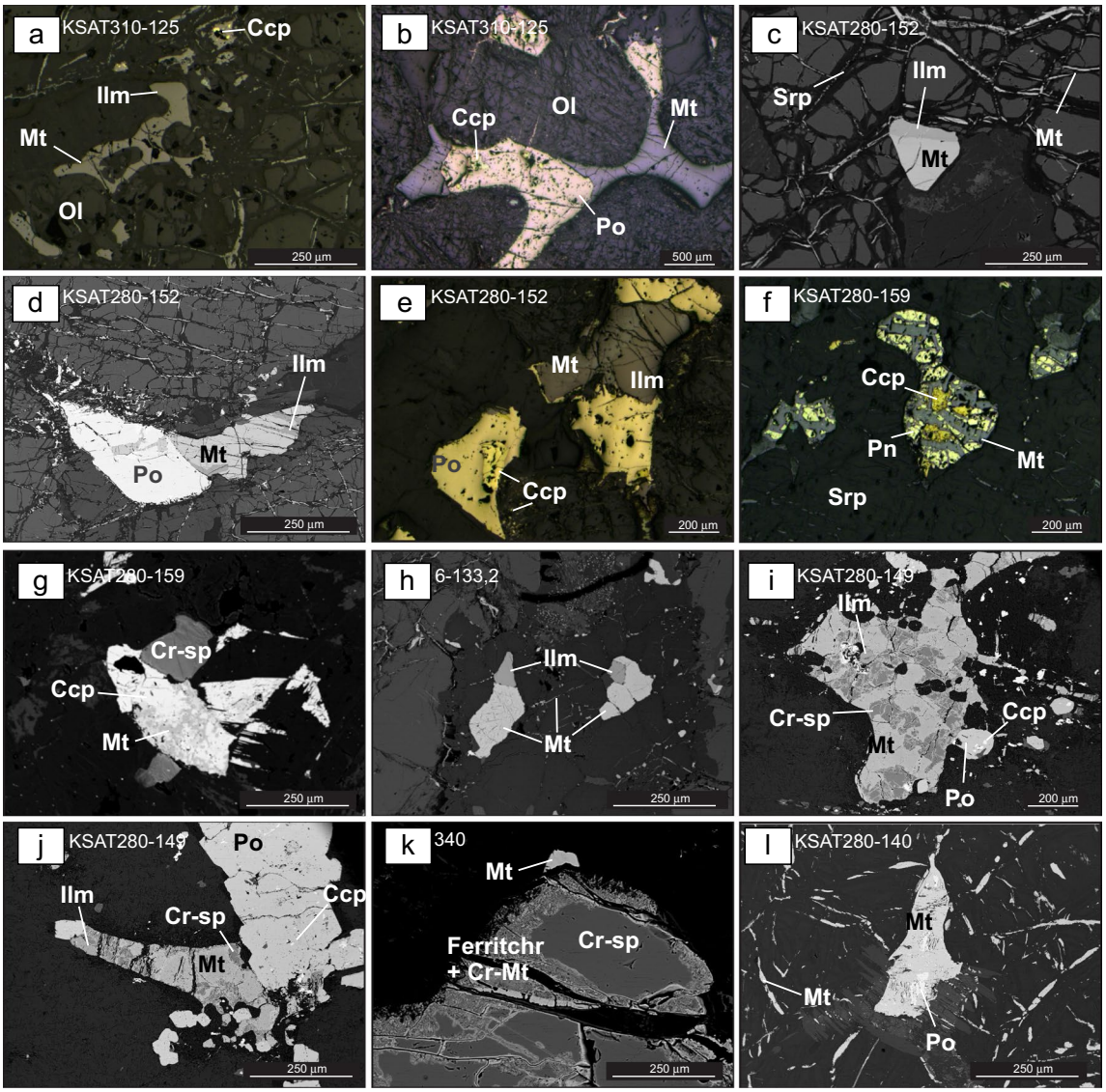

Fig. 3 BSE and reflected light photomicrographs of the main oxide and sulfide minerals of studied samples. **a**-**e**: Troctolite KSAT310-125 and KSAT280-152 (Ohamaremba) showing xenomorphic crystallization of interstitial Fe-Ti-oxide and sulfide between cumulus olivine (a, b), discrete euhedral magnetite with ilmenite (c) and intergrown Fe-Ti-oxides and sulfides (d, e). Magnetite also occurs as veinlets (a, c, d) and chalcopyrite as micrograins (e). **f**–**g**: Secondary magnetite that has replaced sulfide and magnetite in veinlets in altered dunite KSAT280-159 (Ombuku North). **h**: Adjacent magnetite and ilmenite in troctolite 6–133,2 (Ombuku North). **i**, **j**: Cr-spinel, with discrete inclusions of subhedral ilmenite grains, replaced by magnetite in harzburgite KSAT280-149 (Ombuku South). Sulfides are represented by anhedral pyrrhotite with minor chalcopyrite inclusions. **k**: Serpentinite sample 340 (Ombuku South), characterized by large primary Cr-spinel rimmed by Cr-magnetite and ferritchromite. **l**: Harzburgite KSAT280-140 (Onyokohe), with anhedral magnetite including pyrrhotite blebs and magnetite in veinlets. Abbreviations: Ccp = chalcopyrite; Cr-mt = Cr-magnetite, Cr-sp = Cr-spinel, Ferritchr = ferritchromite; Ilm = ilmenite, Mt = magnetite, Ol = olivine, Pn = pentlandite, Po = pyrrhotite, Srp = serpentine

Ohamaremba troctolite KSAT280-152 and Oncócua apatite-orthopyroxenite Onc1-17, Onc1-27 (Zn > 7800 ppm), in Ombuku North serpentinite KSAT280-159 and Onyokohe harzburgite KSAT280-140 (Ni > 26,000 ppm), and in Onyokohe harzburgite KSAT280-140 and Ombuku North serpentinite KSAT280-159 (Cu > 4200 ppm, see ESM4). Cobalt in magnetite is high in Ombuku North serpentinite KSAT280-159 (Co > 900 ppm), in Ohamaremba troctolite KSAT280-125 (Co > 500 ppm), and in Onyokohe norite KSAT280-145 (Co > 300 ppm). However, there is no correlation between olivine-rich rocks and Ni-Co in magnetite, and Fe-oxides in other olivine-bearing samples (for example, troctolite KSAT280-152) retain relatively low Ni and Co. Harzburgite KSAT280-140 (Onyokohe), where only late-stage magnetite has been analyzed, shows consistently high As and Sb contents (a few ppm), whereas these elements in

primary magnetite are commonly below the detection limit. Interestingly, magnetite that replaces sulfide in serpentinite KSAT280-159 at Ombuku North (e.g., Fig. 3f, g) is remarkably different from the other samples as most of the analyzed magnetite grains are depleted in lithophile elements Cr, Ti, V, Mg and Al, but are enriched in chalcophile elements Ni, Cu, Co, Pb, As and Sb. PGE in magnetite are commonly below the detection limit, but in this sample 9 of 17 grains contain appreciable Pd (max. 48 ppm), while elsewhere only low Pt (max. 0.19 ppm) and Pd (max. 0.74 ppm) were measured. This suggests the occasional presence of PGE microinclusions in magnetite.

The concentration of HFSE (Y, Zr, Nb, Hf, Ta) in magnetite is usually below the detection limit, with an exception being the Ohamaremba troctolites, where many magnetite grains are moderately Nb-enriched (up to 1.7 ppm). The rare earth element (REE) content of magnetite is negligible, confirming that magnetite is a minor host for these elements.

The few Cr-magnetites in troctolite KSAT310-125 (Ohamaremba) are enriched in Ti (up to 31,300 ppm), V (up to 6100 ppm), but also in Ni (up to 1300 ppm), Co (up to 530 ppm) and Zn (up to 14,300 ppm). The ferritchromites from harzburgite KSAT280-149 (Ombuku S) show high Ti (up to 24,000 ppm), V (up to 3600 ppm), Ni (up to 1400 ppm), Zn (up to 3400 ppm), and Nb (up to 0.14 ppm).

Discussion

Magnetite types

Magnetite in sulfide-bearing rocks can be formed in multiple ways. An immiscible sulfide liquid segregating from a silicate melt may contain significant amounts of dissolved oxygen, and therefore magnetite can fractionate with MSS (monosulfide solid solution) and ISS (intermediate solid solution) phases (e.g., Naldrett 2004; Dare et al. 2012; Boutroy et al. 2014; Duran et al. 2016b; Ward et al. 2018). This means that in a sulfide-mineralized rock we can expect primary magnetite (Fe_2O_3), sometimes variably Cr-enriched, which crystallized from the silicate and/or the sulfide melt. Moreover, post-magmatic hydrothermal alteration at different temperatures can affect the iron oxide content of a sulfide deposit, causing desulphurization and progressive replacement of sulfides by secondary magnetite (e.g., Konnunaho et al. 2013; Yang et al. 2018; Moilanen et al. 2020), or introducing late-stage, low-temperature magnetite in fractures and microveinlets (e.g., Dare et al. 2014; Nadoll et al. 2014; Milani et al. 2017; Huang et al. 2019; Duran et al. 2020).

Magnetite is present in our samples in various morphologies, sizes and textures and has varying mineral associations. Magnetite textures are disseminated, net-textured and massive, or in veins of various thicknesses (typically below 1 mm). Based on textural criteria, we could define five types of magnetite. Type 1 magnetite is either in contact with or hosted within sulfide grains, or as massive mineralized zones, and is therefore inferred to have formed from the direct fractionation of a sulfide liquid (e.g., Fig. 3e). This type is present at Ohamaremba (KSAT280-152), Oheuwa (KSAT280-144) Ongoro (KSAT280-127 and KSAT280-131), and at Oncócua (Onc1-17 and Onc1-27, see Table 1). Type 2 magnetite is characterized by single or aggregated grains that typically contain ilmenite as discrete crystals or exsolution lamellae. Magnetite is unrelated to sulfides, which in these rocks are generally minor or absent (e.g., Fig. 3c). We therefore interpret Type 2 magnetite to have formed by segregation from silicate liquid. Type 2 is present at Ombuku North (6–133,2), Onyokohe (KSAT280-145) and Oheuwa (KSAT280-143). Type 3 magnetite replaces Cr-spinel, and is therefore inferred to form indirectly from a silicate liquid. It occurs sporadically at Ohamaremba (KSAT310-125) and characterises Ombuku South (KSAT280-149, 340) (e.g., Fig. 3i-k). Type 4 magnetite partially replaces sulfide around fractures or forms selvedges around large blebs of sulfide, and it also occurs as irregular patches within sulfides (e.g., Fig. 3f) or as coronitic rims around sulfides. This type is characteristic of the highly altered (serpentinized) rocks at Ombuku North (KSAT280-159), and to a lesser extent at Onyokohe (KSAT280-140). Type 5 magnetite is represented by stockworks and oriented swarms of veinlets that are typically a few microns thick (e.g., Fig. 3l, where the large magnetite grain is Type 1) and is present at Ohamaremba (KSAT310-125), Ombuku North (6–133,2), and Onyokohe (KSAT280-140). We relate Type 4 and Type 5 magnetite to late-stage hydrothermal fluid circulation rather than magmatic crystallization. A summary of the main geochemical features of the five types is presented in Fig. 6.

Magmatic magnetite: sulfide liquid- (Type 1) and silicate liquid-related (Type 2)

Geochemical affinities and/or discriminants among magnetite types are affected by variations in the chemistry of the parental magmas, the degree of fractionation, the rate of cooling, the sequence of crystallization from a sulfide liquid, and the oxygen fugacity (Dare et al. 2012; Liu et al. 2015).

The textures we have documented indicate that Type 1 magnetite is related to the crystallization of a sulfide liquid and Type 2 magnetite is related to the crystallization of a silicate liquid. Both Type 1 and Type 2 magnetite are enriched in V and Cr compared to bulk continental crust, and depleted in Si, Ca, Y, Pb, Zr, Hf, Nb, Ta and Mg (Fig. 7a). Robust geochemical discriminants between Type 1 and Type 2 magnetite are represented by Ni and Co, which are higher in the magnetite crystallized from a silicate liquid (Fig. 8). Numerous studies have been published on the metal–silicate

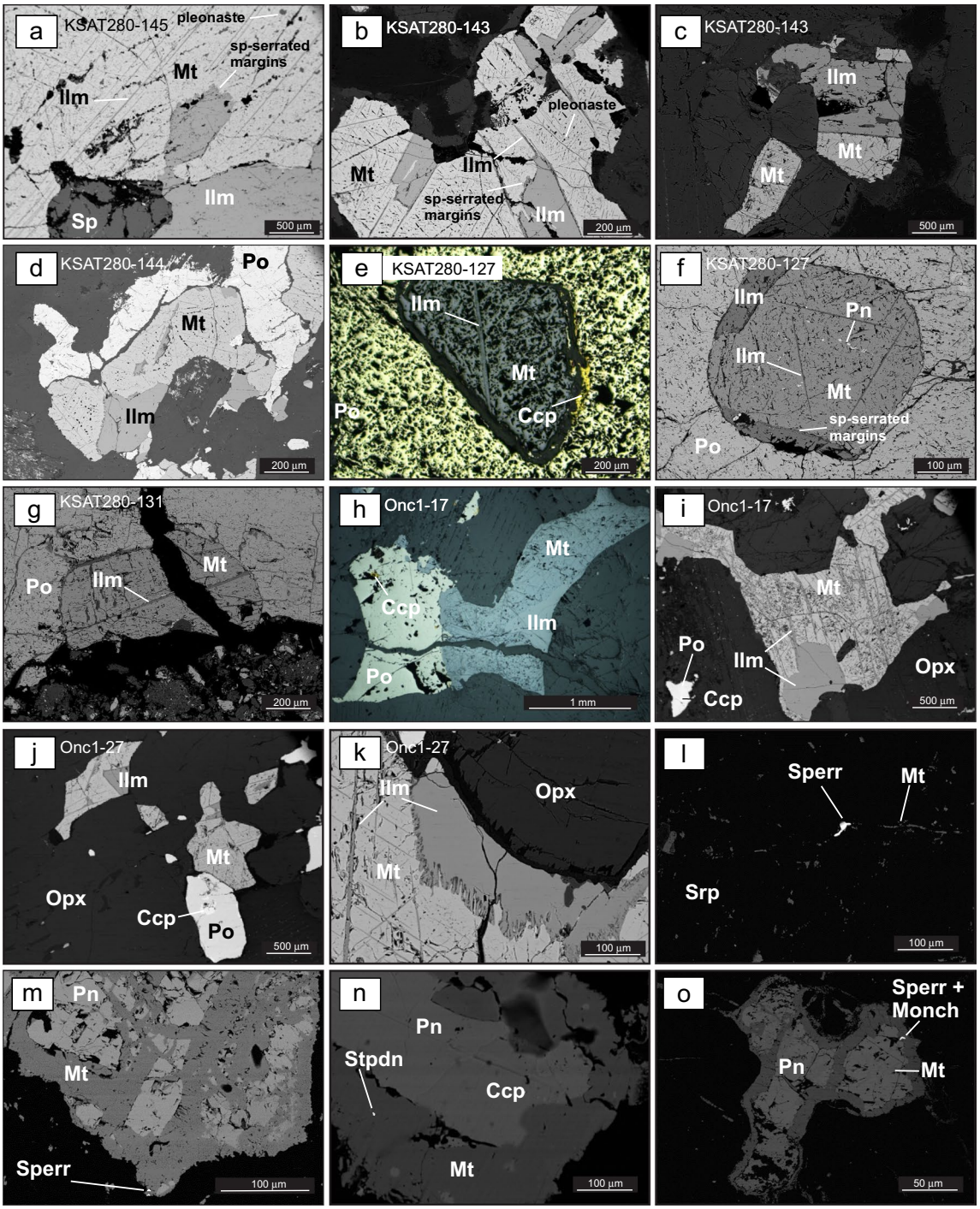

partitioning coefficients of Ni and Co, and on the distribution of Ni between olivine, pyroxene and silicate melt (Mysen 1978; Hirschmann and Ghiorso 1994; Sobolev et al. 2005; Kegler et al. 2008; Li and Ripley 2010; Dare et al. 2012; Matzen et al. 2013). The production of high-Ni melts and the availability of free Ni (and Co) in a silicate liquid, which can partition into magnetite, depend on factors like the composition of the melt (olivine-bearing or olivine-free), metasomatism, temperature, pressure and oxygen fugacity (e.g., Mysen and Kushiro 1979; Kinzler et al. 1990; Hirschmann and Ghiorso 1994; Matzen et al. 2013). The siderophile behaviour of Ni and Co and the mechanisms by which these elements enter the Fe-oxide crystal structure are beyond the scope of this work. However, what is relevant is that our data show that Type 1 magnetite is relatively depleted in Ni-Co (Fig. 7a). Considering the high to moderate sulfide/silicate liquid partition coefficients for Ni and Co, which will preferentially partition the elements into the sulfide liquid (e.g.,

◂**Fig. 4** BSE and reflected light photomicrographs of the main oxide and sulfide minerals of studied samples. **a**: Large grains of magnetite, ilmenite and spinel in norite KSAT280-145 (Onyokohe). Also visible are spineliferous serrated margins at the magnetite–ilmenite contact, as well as pleonaste spinel and ilmenite exsolution lamellae in magnetite. **b**, **c**: Magnetite intergrown with euhedral ilmenite in olivine norite KSAT280-143 (Oheuwa), with serrated spinel-lined margins. Magnetite is punctuated by pleonaste spinel micro-inclusions and shows cloth texture and trellis-type ilmenite exsolution. **d**: Fe-Ti-oxide and sulfide pyrrhotite association in websterite KSAT280-144 (Oheuwa). **e**–**g**: Discrete euhedral oxy-exsolved magnetite grains in pyrrhotite in pyroxenite KSAT280-127 and KAST280-131 (Ongoro). Exsolved ilmenite lamellae are common along the [111] of magnetite, and the Mt/Ilm boundary is marked by spinel micro-grain chains as serrated margins (r). **h**-**j**: Magnetite–ilmenite exsolution, intergrown with (h), or in close association with (i, j), pyrrhotite (±chalcopyrite and pentlandite) and interstitial to orthopyroxene in apatite-orthopyroxenites of Onc1-17 and Onc1-27 (Oncócua). Ilmenite is visible as elongated sectors or thin trellis lamellae in magnetite. **k**: fringed reaction boundary between ilmenite and magnetite in apatite-orthopyroxenite Onc1-27. l-o: from Ombuku North (samples not in table list), **l**: elongated sperrilyte ($PtAs_2$) flakes up to 40 μm embedded in altered dunite (serpentinite). **m**–**o**: µm-size sperrylite, stibiopalladinite (Pd_5Sb_2), and moncheite ($(PtPd(TeBi)_2$) in Type 4 magnetite. Abbreviations: Ap = apatite, Ccp = chalcopyrite; Ilm = ilmenite, Mt = magnetite, Monch = moncheite, Opx = orthopyroxene, Pn = pentlandite, Po = pyrrhotite, Sperr = sperrylite, Srp = serpentine, Stpdn = stibiopalladinite

MacLean and Shimakazi 1976; Gaetani and Grove 1997; Lee et al. 2012; Li and Audétat 2012), this suggests that the low Ni-Co content of Type 1 magnetite is due to these elements being sequestered in sulfides (in particular pentlandite) co-crystallising with Fe-oxides.

Sulfide liquid fractionation

Type 1 magnetite shows a relatively wide range of Mo, Sn, Ti, Co, Ni, and Cr relative to bulk continental crust, with many Type 1 magnetite grains having lower concentrations of these elements compared to Type 2 magnetite (Fig. 7a). This could be ascribed to the degree of fractionation of the sulfide liquid, or to chemical heterogeneity in the magma prior to the segregation of the immiscible sulfide or silicate liquids.

During the crystallization of a sulfide melt, the lithophile elements (including Ti and Cr) are strongly compatible with magnetite and tend to concentrate in early Fe-oxides in the MSS, leading to their depletion in the remaining Cu-enriched ISS (e.g., Dare et al. 2012, 2014). Type 1 magnetite shows positive spikes in Cr, V and, although less pronounced, in Ti (Fig. 7a). The chalcophile elements (Pb, Cu, Mo, Sn, Mn, Zn, Co, Ni) will be sequestered by the crystallising sulfide liquid so that magnetite will be depleted in these elements, with concentrations typically below the detection limits. Copper, Pb, and Sn are compatible with the Cu-rich ISS, whilst Ni, Co and Mo tend to concentrate in the Fe-rich MSS, and the latter elements will therefore be depleted in magnetite crystallized from MSS (Dare et al. 2012). The remaining Ni, Co, and Mo in the sulfide melt during the segregation of the ISS behave incompatibly with the crystallising sulfides, and therefore magnetite crystallising from the late-stage ISS will be enriched in the elements (Dare et al. 2012). The behaviour of chalcophile elements in Type 1 magnetite does not necessarily follow a theoretical behaviour: Pb and Cu are commonly depleted compared to the continental crust, but Mo, Sn, Mn, and Zn are quite variable, ranging from sub-crustal values to tenths of continental crust units. Zinc concentration ranges from below 1 ppm to thousands of ppm, suggesting the presence of possible microinclusions in magnetite (Fig. 7a). Type 1 magnetite also shows depletion in HFSE (Nb, Ta, Zr, Hf), and variable Ti, with contents of > 1–2 wt% in apatite-pyroxenite at Oncócua but mostly < 0.5 wt% at Ohamaremba and Ongoro (see ESM 4). These variations in HFSE-Ti are likely due to the timing of ilmenite crystallization, as these elements (along with Mg, Sc, W) will preferentially partition into ilmenite when it co-crystallises with magnetite, such as for example in the Lac des Îles intrusion of Canada (Duran et al. 2016b). The relatively low Ni and Co contents of Type 1 magnetite, besides providing a discriminant between the two magmatic types (Fig. 8), suggest that the sulfide liquid in all the mafic–ultramafic intrusions was likely to have comprised predominantly unfractionated MSS. This conclusion is supported by the binary plots in Fig. 9a, b, where the high Cr, V and Ti contents of Type 1 magnetite indicate that it crystallized from a primitive MSS (Dare et al. 2012; Boutroy et al. 2014). This is not unusual: among some of the world-class Ni-Cu-PGE sulfide deposits (e.g., Sudbury, Voisey's Bay and Lac des Îles in Canada, Noril'sk-Talnakh in Russia, Munali in Zambia, the Fennoscandian deposits in Finland), magnetite preserves a record of crystallization from MSS with a lack of extensive fractional crystallization of the sulfide liquid towards ISS compositions (e.g., Duran et al. 2020, and references therein; Moilanen et al. 2020).

Type 3 magnetite: High-T replacement of Cr-spinel

Cr-spinel (chromite) and Cr-rich magnetite (ferritchromite, Cr-magnetite) may crystallise from a silicate melt or as primary phases from a sulfide liquid (Frost and Groves 1989; Fonseca et al. 2008; Moilanen et al. 2020). Secondary Cr-rich oxides are also common and may result from metamorphic events spanning a wide range of conditions that combine solid-state and hydrothermal processes (e.g., Merlini et al. 2009; Ahmed and Surour 2016; Hodel et al. 2020, and references therein; Moilanen et al. 2020). Chromite, here defined as chromium-spinel, has been documented in the cumulates of the Ombuku North and South intrusions, and occurs as xenomorphic crystals, as discrete grains or in association with sulfides (e.g., Fig. 3g, i, j, k).

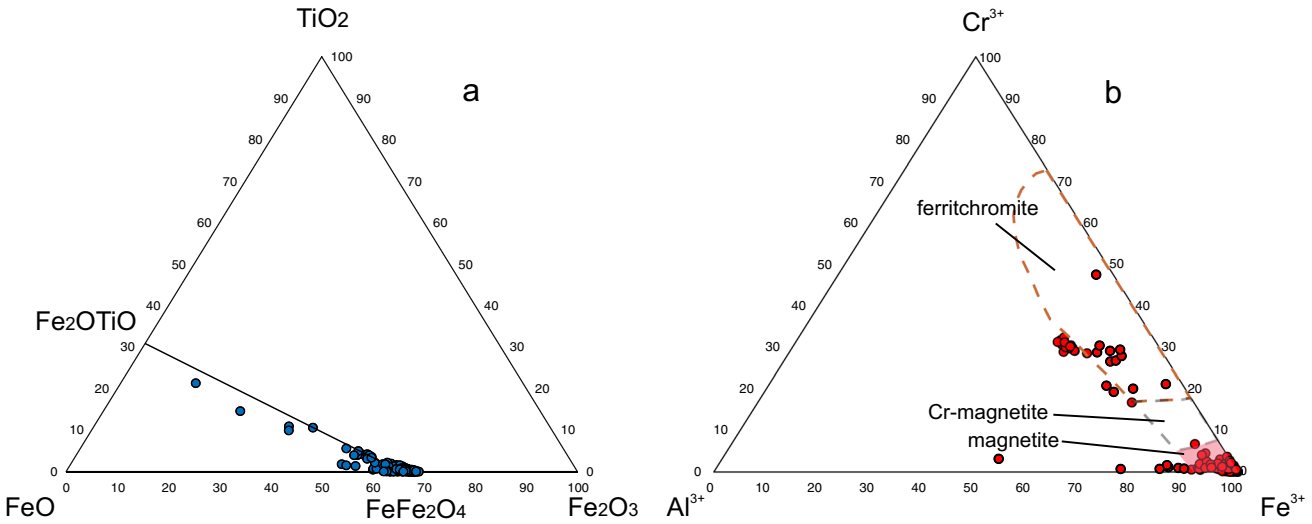

Fig. 5 **a**. Ternary plot of the 'magnetite series' solid solution array between magnetite ($Fe^{2+}Fe_2^{3+}O_4$), magnesioferrite ($MgFe_2O_4$) and ulvöspinel (Fe_2TiO_4). **b**. Ternary plot of the Cr-Al-Fe.$^{3+}$ cation end-members for spinel with the compositions of magnetite, Cr-magnetite and ferritchromite from the sampled intrusions. The compositional fields are from Barnes and Roeder (2001)

At Ombuku South, massive chromite is present in lenses up to a few meters thick (Naumov 2008; Maier et al. 2013). In our samples, Cr-magnetite and ferritchromite were analyzed in harzburgite from Ombuku South (KSAT280-149) and troctolite from Ohamaremba (KSAT310-125) (Fig. 5, Table 3, ESM4). Ferritchromite and Cr-magnetite are present as patches in Cr-spinel or as replacement rims around Cr-spinel (Fig. 3i-k). This textural relationship suggests that the Cr-rich magnetite formed by the alteration of primary magmatic Cr-spinel.

The trace elements of Type 3 magnetite show variable contents of Cu, Mo and Co, and enrichment in Sn, Ni, and especially Zn, relative to bulk continental crust (Fig. 7b). Enrichment in Zn supports the hypothesis that the Type 3 magnetite formed by the alteration of Cr-spinel (e.g., Barnes 2000). Mn, Ti, V, and Cr are enriched, whereas Hf, Zr, Nb, Ta, Ga, and Mg are notably depleted. As for the conditions responsible for the alteration and development of Cr-rich magnetite, the presence of wide Fe-rich alteration rims (Fig. 3k) may suggest relatively high-temperature fluids (500–600 °C or higher; Mellini et al. 2005; González-Jiménez et al. 2009; Ahmed and Surour 2016). Moreover, Cr-magnetite from lower-T hydrothermal environments typically does not contain Ti as high as 2000 ppm, while in our case the Ti content in the Ohamaremba Cr-magnetite is 10 times higher (see ESM4) and so we suggest that a secondary high-T event may be responsible for the Type 3 magnetite. However, this remains a controversial topic, as diffuse patchy textures in chromite (Fig. 3i), as well as zonation, have typically been attributed to low-metamorphic and low-temperature processes (e.g., Marques et al. 2007; Saumur and Hattori 2013; Barra et al. 2014; Hodel et al. 2017). A more detailed microtextural study may be useful to clarify the paragenesis of Type 3 magnetite.

Magmatic vs. hydrothermal magnetite

Two distinct types of hydrothermal magnetite have been observed: Type 4, formed by the progressive replacement of sulfides (Fig. 3f), and Type 5, which forms tiny crystals and veinlets (Fig. 3l) and appears to be the product of low-T hydrothermal fluids at a late stage. Both Type 4 and Type 5 magnetite show strong depletion in Al, Ti, Cr and V (Fig. 7c) compared to the magmatic magnetite types (Fig. 7a). The partitioning behaviour and concentrations of some of these elements in magnetite (e.g., Ti, V, Cr), as well as Ni, has been used as a discriminant between magmatic and hydrothermal environments (Nadoll et al. 2014) and dedicated diagrams to assess the relative roles of these processes have been developed (e.g., Ni/Cr vs Ti of Dare et al. 2014). In hydrothermal fluids, Ni is likely more soluble than Cr (e.g., Dare et al. 2014) therefore Ni/Cr is one of the most robust parameters to identify low-temperature magnetite. The magmatic (Types 1 and 2) and high-T replacement (Type 3) magnetite show greater concentrations of Ti at relatively lower Ni/Cr compared to the hydrothermal magnetite (Types 4 and 5), which show lower concentrations of Ti at higher Ni/Cr (Fig. 10a).

Titanium and V contents of magnetite are also powerful tools to fingerprint petrogenetic environments (Dare et al. 2012; Zhou et al. 2013; Nadoll et al. 2014; Liu et al. 2015). Magmatic magnetite is typically Ti-enriched compared with hydrothermal magnetite, which is commonly depleted (Ti < < 1 wt%), and this may in part be related

Table 2 Representative EPMA analyses (in ppm) of magnetite (Mt), Cr-magnetite (Cr-Mt) and ferritchromite (Ferritchr). Ol = olivine; Ap = apatite. Late-stage hydrothermal magnetite veinlets are indicated separately. n.d. = not detected. Total (as wt%) was calculated assuming the O stoichiometric value of 27.60 wt%

Intrusion	Ohamaremba					Ombuku North		Ombuku South			
Sample	KSAT310-125			KSAT280-152		6–133,2	KSAT280-159	KSAT280-149		340	
Rock type	Troctolite			Troctolite		Troctolite	Serpentinite	Harzburgite		Serpentinite	
Mineral	Mt	Cr-Mt	Ferritchr	Mt	Mt veinlets	Mt	Mt	Mt	Ferritchr	Mt	Ferritchr
	avg ($n=6$)	avg ($n=4$)	avg ($n=2$)	avg ($n=7$)	avg ($n=7$)	avg (n = 13)	avg ($n=9$)	avg ($n=3$)	avg ($n=17$)	avg ($n=7$)	avg ($n=5$)
Si	2664	222	164	187	8027	2362	774	2540	775	3432	103
Ti	490	16,471	24,490	1584	694	8642	187	1499	14,495	942	26,522
Al	88	26,595	27,574	794	136	4356	12	300	25,592	151	18,767
Cr	296	80,548	117,033	2825	10	4853	859	11,837	96,306	4545	114,152
V	23	7460	6900	5720	10	4073	23	476	2506	233	3358
Fe3 +	469098	310109	254257	468423	451680	435377	475327	462296	304577	459059	266224
Fe2 +	239739	252186	264627	242098	246849	294434	239608	250220	256311	238948	254501
Mn	n.d	1897	3059	n.d	66	751	155	181	6096	111	13,863
Mg	2563	3271	3136	749	5066	2231	583	181	1959	1094	1797
Ca	155	339	71	31	511	379	183	48	46	378	43
Ni	681	825	1375	202	247	689	288	786	998	6287	2515
Zn	80	7411	4338	92	46	99	45	54	907	34	3230
Co	118	452	590	34	101	175	52	26	63	56	157
O	276000	276000	276000	276000	276000	276000	276000	276000	276000	276000	276000
Total	99.20	98.38	98.36	99.87	98.94	98.94	99.41	100.64	98.66	99.13	98.12

Table 2 (continued)

Intrusion	Onyokohe		Oheuwa		Ongoro		Oncócua	
Sample	KSAT280-145	KSAT280-140	KSAT280-143	KSAT280-144	KSAT280-127	KSAT280-131	Onc1-17	Onc1-27
Rock type	Norite	Harzburgite	Ol-norite	Websterite	Pyroxenite	Pyroxenite	Ap-pyroxenite	Ap-pyroxenite
Mineral	Mt	Mt	Mt	Mt	Mt	Mt	Mt	Mt
	avg ($n=13$)	avg ($n=21$)	avg ($n=10$)	avg ($n=14$)	avg ($n=14$)	avg ($n=10$)	avg ($n=28$)	avg ($n=28$)
Si	269	4091	234	317	290	252	3324	2973
Ti	1308	194	9119	2651	360	534	13,791	14,371
Al	2515	40	5293	2661	1527	1514	5710	9239
Cr	269	49	12,678	689	3631	5275	1312	3421
V	2654	65	9204	1787	1753	2406	3392	5152
Fe3+	471741	464651	427310	466567	470483	468615	425513	416254
Fe2+	242663	244894	250697	243460	240910	241416	260109	261298
Mn	n.d	225	751	33	144	232	788	656
Mg	400	1381	308	211	73	145	2096	2121
Ca	8	398	107	342	296	79	528	235
Ni	600	292	416	146	73	134	73	132
Zn	46	38	554	287	34	72	100	473
Co	115	82	149	62	39	71	56	81
O	276000	276000	276000	276000	276000	276000	276000	276000
Total	99.86	99.24	99.28	99.52	99.56	99.67	99.28	99.24

Table 3 Summary of LA-ICP-MS average composition (in ppm) and standard deviation of magnetite (Mt), Cr-magnetite (Cr-Mt) and ferritchromite (Ferritchr) for the studied intrusions

Intrusion	Ohamaremba						Ombuku North				Ombuku South		Onyokohe	
Sample	KSAT310-125				KSAT280-152		6,133–2		KSAT280-159		KSAT280-149		KSAT280-140	
Rock type	Troctolite				Troctolite		Troctolite		Serpentinite		Harzburgite		Harzburgite	
Mineral	Mt		Cr-Mt		Mt		Mt		Mt		Ferritchr		Mt	
	avg (n = 8)	Stdev	avg (n = 5)	Stdev	avg (n = 11)	Stdev	avg (n = 8)	Stdev	avg (n = 10)	Stdev	avg (n = 22)	Stdev	avg (n = 24)	Stdev
Na	141	343	8.79	7.52	15.4	13.4	287	789	12.6	14.4	24.1	30.3	39.5	23.0
Mg	13,429	8348	7405	5215	5843	5432	3060	3122	1833	3454	4022	2442	7079	8646
Al	2092	5468	25,106	1774	3849	3323	9021	3778	42.3	61.0	26,361	5510	179	166
Si	15,287	6833	6545	10,651	3240	5074	10,838	9156	916	4264	2635	4808	9730	6427
P							80.7				11.1	4.62	163	337
K	83.9	105	4.81	6.54	11.1	26.0	396.2	673	4.06	7.81	10.6	16.7	7.49	9.92
Ca	1545	1214	148	212	598	2197	2633	3267	339		102	399	695	752
Sc	1.32	0.370	3.13	1.04	2.30	1.12	3.91	3.96	0.166	0.172	8.87	2.76	0.760	0.5
Ti	433	228	23,980	1382	3350	3718	15,339	7038	190	100	13,179	3163	218	95.3
V	28.0	55.4	4546	374	5708	3312	5018	1552	28.2	22.9	2188	365	72.9	43.1
Cr	61.5	75.6	68,243	4101	3008	1428	4995	1710	78.7	179	92,520	12,174	13.4	35.1
Mn	210	245	1854	148	349	187	1359	411	398	95.1	5608	958	517	122
Co	221	163	398	23.4	35.3	17.7	156	18.9	60.1	63.1	34.2	29.3	53.1	33.6
Ni	1319	1060	824	260	180	112	950	79	1521	1798	780	88.2	289	149
Cu	72.0	86.1	0.650	0.113	208	408	4.22	5.00	672	856	47.7	74.4	8	47.8
Zn	117	151	9267	2531	614	795	251	313	7.20	4.20	960	626	17.4	8.2
Ga	0.292	0.351	10.9	1.83	3.46	1.45	11.3	1.84	0.126	0.096	7.31	3.59	0.155	0.108
Ge	2.40	0.777	0.749	0.151	2.03	1.05	2.21	0.433	1.67	0.208	1.05	0.132	1.49	0.494
As									0.097	0.043	0.035	0.038	1.09	1.50
Y	0.204	0.139	0.198	0.153	0.443	0.437	1.30	2.85	0.352	0.268	0.020	0.030	0.582	0.442
Zr	1.43	1.63	1.67	1.15	3.30	5.64	3.56	8.01	2.84	1.92	0.182	0.071	0.377	0.461
Nb	0.109	0.088	0.157	0.135	0.465	0.529	0.320	0.697	0.003	0.002	0.074	0.021	0.047	0.057
Mo	0.081	0.060	1.77	0.284	0.434	0.585	7.31	3.11	0.012	0.061	0.069	0.041	0.027	0.022
Pd	0.088	0.042	0.005		0.124	0.252	0.027		5.35	13.0	0.012	0.014	0.012	0.068
Sn	0.305		4.72	1.12	2.16	3.22	2.74	0.590	0.135	0.183	6.38	3.81	0.015	
Sb									1.58	3.07	0.008		0.466	0.388
La	0.493	0.321	0.058	0.043	0.452	0.574	0.184	0.320	1.01	0.682	0.045	0.071	1.41	1.51
Ce	0.808	0.449	0.118	0.084	0.985	1.22	0.754	1.22	1.55	0.990	0.078	0.131	2.81	2.66
Pr	0.104	0.073	0.014	0.005	0.143	0.186	0.160	0.247	0.156	0.093	0.007	0.016	0.318	0.273
Nd	0.365	0.365	0.053	0.034	0.525	0.945	0.784	1.42	0.584	0.395	0.020	0.034	1.10	0.940
Sm	0.143	0.119	0.008		0.043	0.159	0.292	0.517	0.147	0.124	0.005	0.009	0.176	0.137
Eu	0.051	0.014	0.006	0.010	0.024	0.044	0.094	0.145	0.015	0.022	0.003	0.002	0.120	0.076

Table 3 (continued)

Intrusion	Ohamaremba						Ombuku North				Ombuku South		Onyokohe	
Sample	KSAT310-125				KSAT280-152		6,133–2		KSAT280-159		KSAT280-149		KSAT280-140	
Rock type	Troctolite				Troctolite		Troctolite		Serpentinite		Harzburgite		Harzburgite	
Mineral	Mt		Cr-Mt		Mt		Mt		Mt		Ferritchr		Mt	
	avg (n = 8)	Stdev	avg (n = 5)	Stdev	avg (n = 11)	Stdev	avg (n = 8)	Stdev	avg (n = 10)	Stdev	avg (n = 22)	Stdev	avg (n = 24)	Stdev
Gd	0.114	0.043	0.021	0.031	0.099	0.171	0.255	0.395	0.154	0.081	0.007	0.013	0.162	0.104
Tb	0.019	0.012	0.003	0.002	0.030	0.034	0.073	0.122	0.025	0.022	0.001	0.002	0.030	0.020
Dy	0.153	0.208	0.025	0.028	0.116	0.165	0.444	0.564	0.097	0.061	0.006	0.003	0.135	0.112
Ho	0.016	0.010	0.006	0.001	0.038	0.065	0.059	0.088	0.019	0.010	0.002	0.003	0.034	0.034
Er	0.036	0.022	0.021	0.022	0.038	0.064	0.153	0.318	0.060	0.056	0.005	0.012	0.089	0.092
Tm	0.013		0.002		0.013	0.015	0.035	0.055	0.013	0.010	0.001	0.001	0.012	0.021
Yb	0.105	0.115	0.048	0.019	0.042	0.061	0.469	0.503	0.059	0.041	0.003	0.007	0.071	0.072
Lu	0.022	0.008	0.011	0.007	0.011	0.020	0.045	0.062	0.006	0.010	0.000	0.001	0.010	0.011
Hf	0.045	0.016	0.099	0.047	0.331	0.592	0.116	0.189	0.056	0.061	0.029	0.024	0.008	0.079
Ta	0.023	0.024	0.008	0.006	0.004	0.017	0.106				0.003	0.003	0.001	0.006
Re	0.019				0.012	0.055	0.011	0.0003	0.002		0.003	0.017		
Pt					0.014		0.049				0.004	0.004	0.009	0.020
Au														
Pb	0.929	0.879	0.078	0.042	1.98	1.52	0.639	0.488	4.08	2.77	0.591	0.799	3.39	2.94
Th	0.120	0.121	0.021	0.022	0.048	0.074	0.110	0.143	0.009		0.002	0.017	0.033	0.057
U	0.060	0.047	0.005	0.005	0.006	0.017	0.023	0.011			0.004	0.006	0.023	0.044
S REE	2.44		0.395		2.56		2.22		3.89		0.183		6.48	
(La/Yb)N	3.16		0.811		7.23		0.926		11.6		10.0		13.4	
(Gd/Yb)N	0.879		0.352		1.91		1.10		2.11		1.84		1.84	
(La/Sm)N	2.17		4.44		6.60		0.554		4.33		5.33		5.05	

Table 3 (continued)

Intrusion			Oheuwa				Ongoro				Oncócua			
Sample	KSAT280-145		KSAT280-143		KSAT280-144		KSAT280-127		KSAT280-131		Onc 1–17		Onc 1–27	
Rock type	Norite		Ol-norite		Websterite		Pyroxenite		Pyroxenite		Ap-pyroxenite		Ap-pyroxenite	
Mineral	Mt		Mt		Mt		Mt		Mt		Mt		Mt	
	avg (n = 17)	Stdev	avg (n = 20)	Stdev	avg (n = 20)	Stdev	avg (n = 16)	Stdev	avg (n = 18)	Stdev	avg (n = 17)	Stdev	avg (n = 21)	Stdev
Na	4.32	7.76	31.1	30.7	19.5	68.2	22.2	38.9	7.02	7.81	31.4	22.1	4.17	7.43
Mg	1587	1080	2391	3010	1180	1688	288	422	170	160	4848	3048	2438	1316
Al	8800	3713	10,052	2979	7539	2646	2784	903	2650	626	8028	3079	11,564	5231
Si	112		2105	3435	2414	4947	1285	2409	127	91.7	6658	4791	2292	3169
P	3.88						13.4	28.8			6.10		19.6	19.6
K	0.450		15.1	42.7	9.26	46.2	15.2	73.8	3.38	12.9	16.76	15.2	2.32	6.06
Ca	30.0		249	1622	47.0	330	796	862			1760	4418	16.6	39.5
Sc	1.74	0.896	2.18	1.12	2.08	1.88	0.765	0.343	0.941	0.175	4.59	2.54	4.31	2.64
Ti	14,857	15,275	21,634	10,513	6184	6922	4493	12,706	683	271	17,130	12,179	25,131	27,539
V	2501	158	7998	4030	1844	133	1702	565	2544	120	3615	885	5496	1305
Cr	297	31.4	11,930	4694	833	127	3800	985	5300	324	1489	674	3436	1444
Mn	469	335	1813	850	294	226	993	1767	562	125	1306	886	1297	1142
Co	150	57.5	97.9	46.9	35.0	17.2	13.1	2.14	13.1	1.52	30.5	16.7	37.5	14.0
Ni	635	73.6	448	69.9	147	26.6	117	37.4	114	13.7	96.3	36.5	94.9	21.1
Cu	1.14	1.71	1.57	1.18	0.356	0.455	1.03	1.42	0.797	0.8	62.3	171	43.4	91.2
Zn	70.5	59.7	713	689	321	389	253	580	57.1	50.4	244	244	853	1593
Ga	13.7	1.60	15.3	6.96	17.7	4.36	11.9	5.33	12.5	2.74	18.1	3.27	25.7	4.32
Ge	1.60	0.315	2.08	0.489	2.22	0.520	1.72	0.253	1.80	0.356	3.46	0.610	2.75	0.769
As	0.017		0.188	0.160	0.065	0.101	0.066	0.042			0.061	0.142	0.008	
Y	0.037	0.142	0.130	0.380	0.292	0.824	0.866	2.80	0.015	0.035	1.81	1.85	0.069	0.112
Zr	0.546	0.401	1.11	1.11	0.314	0.395	0.092	0.223	0.044	0.033	1.43	1.137	1.80	3.68
Nb	0.019	0.050	0.024	0.017	0.004	0.012	0.031	0.183	0.008	0.010	0.016	0.038	0.211	1.09
Mo	12.1	2.30	1.37	0.814	4.79	2.20	0.216	0.117	0.287	0.163	1.67	0.737	1.64	0.486
Pd	0.028	0.083	0.004		0.015	0.025	0.016	0.039	0.018	0.031	0.010	0.011	0.004	0.008
Sn	12.1	1.95	4.57	1.99	5.29	2.24	4.68	3.05	1.93	1.26	1.62	1.24	5.67	2.07
Sb			0.125	0.079										
La	0.013	0.055	0.050	0.074	0.023	0.070	0.066	0.196	0.011	0.021	0.369	0.438	0.042	0.096
Ce	0.054	0.278	0.078	0.136	0.053	0.129	0.188	0.535	0.013	0.011	1.24	1.34	0.058	0.105
Pr	0.005	0.050	0.011	0.041	0.014	0.037	0.036	0.141	0.001		0.214	0.217	0.005	0.016
Nd	0.042	0.340	0.047	0.176	0.043	0.161	0.166	0.754	0.012	0.008	1.10	1.15	0.045	0.074

Table 3 (continued)

Intrusion			Oheuwa				Ongoro				Oncócua			
Sample	KSAT280-145		KSAT280-143		KSAT280-144		KSAT280-127		KSAT280-131		Onc 1–17		Onc 1–27	
Rock type	Norite		Ol-norite		Websterite		Pyroxenite		Pyroxenite		Ap-pyroxenite		Ap-pyroxenite	
Mineral	Mt		Mt		Mt		Mt		Mt		Mt		Mt	
	avg (n = 17)	Stdev	avg (n = 20)	Stdev	avg (n = 20)	Stdev	avg (n = 16)	Stdev	avg (n = 18)	Stdev	avg (n = 17)	Stdev	avg (n = 21)	Stdev
Sm	0.017	0.044	0.013	0.074	0.020	0.036	0.055	0.217	0.020	0.047	0.324	0.313	0.015	0.031
Eu	0.006	0.006	0.011	0.046	0.005	0.012	0.051	0.159	0.010	0.051	0.079	0.085	0.004	0.019
Gd	0.017	0.027	0.013	0.036	0.039	0.094	0.097	0.389	0.011	0.048	0.326	0.313	0.018	0.043
Tb	0.003	0.004	0.003	0.035	0.007	0.014	0.017	0.088	0.003	0.007	0.072	0.067	0.003	0.005
Dy	0.015	0.041	0.025	0.102	0.043	0.178	0.159	0.954	0.015	0.022	0.374	0.362	0.011	0.019
Ho	0.002	0.012	0.009	0.031	0.009	0.023	0.027	0.108	0.002	0.002	0.076	0.073	0.003	0.007
Er	0.008	0.013	0.021	0.068	0.045	0.136	0.067	0.268	0.006	0.009	0.213	0.200	0.011	0.026
Tm	0.002	0.005	0.003	0.009	0.006	0.015	0.015	0.052	0.002	0.003	0.029	0.031	0.002	0.006
Yb	0.013	0.023	0.023	0.043	0.047	0.176	0.074	0.294	0.011	0.010	0.189	0.156	0.013	0.049
Lu			0.005	0.018	0.008	0.033	0.007	0.025	0.002	0.002	0.023	0.026	0.003	0.014
Hf	0.082	0.078	0.048	0.052	0.023	0.050	0.010	0.018	0.010	0.024	0.062	0.082	0.086	0.166
Ta	0.003	0.003	0.001	0.001	0.002	0.002	0.003	0.003	0.001	0.003	0.002	0.002	0.005	0.038
Re	0.005	0.017	0.003	0.005	0.004	0.010	0.004	0.001	0.002		0.024	0.180	0.001	0.0004
Pt									0.011		0.014	0.007		
Au									0.035				0.027	
Pb	1.34	1.78	1.74	3.34	0.179	0.179	1.64	1.65	3.88	4.59	0.301	0.408	0.165	0.265
Th	0.002	0.009	0.002	0.001	0.003	0.019	0.010		0.004	0.013	0.029	0.035	0.012	0.051
U	0.003	0.005	0.002	0.003	0.004	0.004	0.010	0.096	0.001		0.005	0.006	0.006	0.015
S REE	0.195		0.313		0.361		1.02		0.118		4.63		0.234	
(La/Yb)N	0.632		1.47		0.327		0.598		0.682		1.32		2.11	
(Gd/Yb)N	0.994		0.458		0.670		1.06		0.786		1.40		1.12	
(La/Sm)N	0.460		2.48		0.702		0.750		0.354		0.716		1.72	

In magnetite ^{57}Fe was assumed with stoichiometric values of 72.4 wt%. In Cr-magnetite and ferritchromite ^{57}Fe is according to EPMA average data (KSAT310-125: ^{57}Fe in Cr-Mt = 46.5 wt%; KSAT280-149: ^{57}Fe in Ferritchr = 37.4 wt%). Silica might be overestimated due to the high background signal. Chondrite REE normalization values after Boynton (1985)

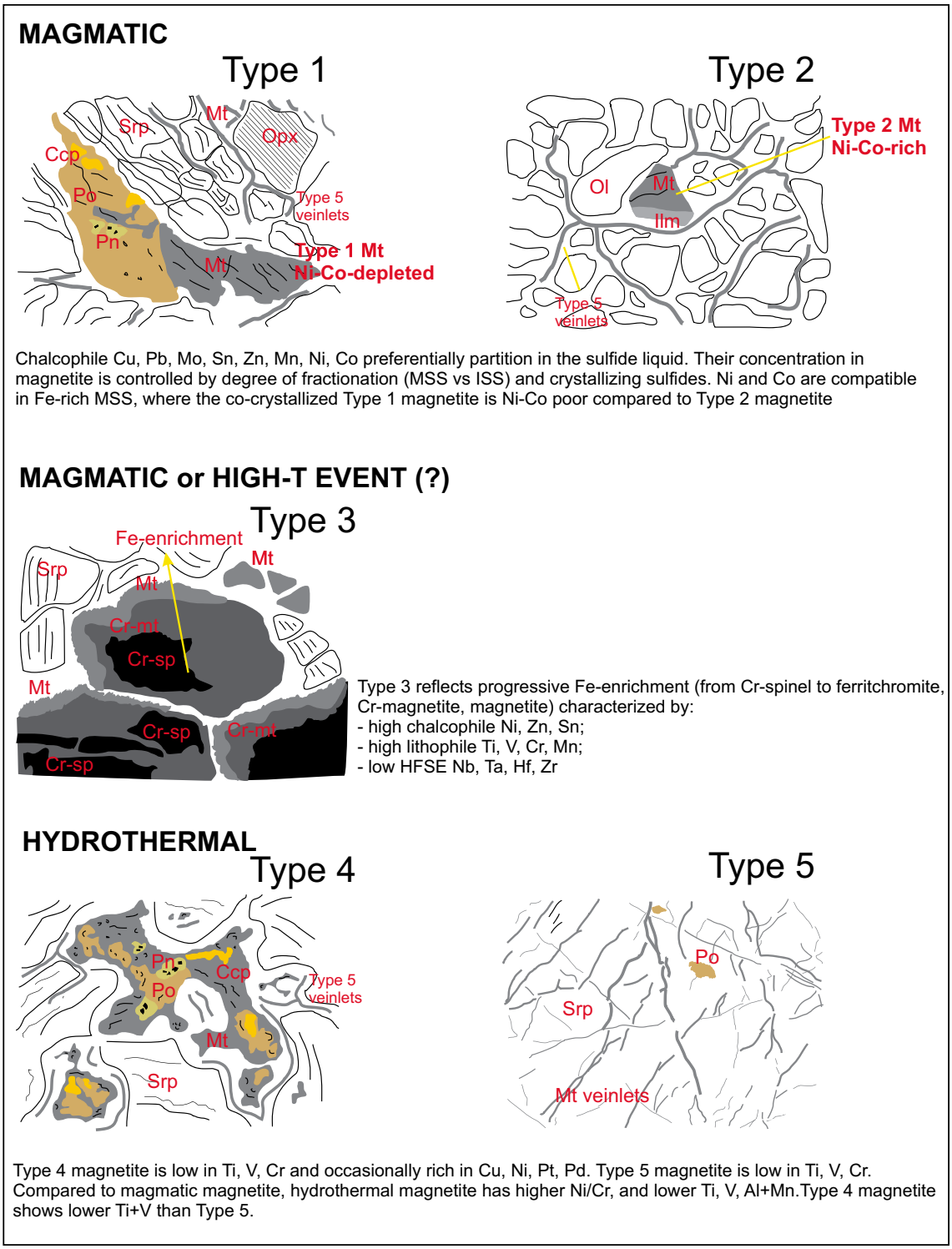

Fig. 6 Schematic representation of the five magnetite types with main distinctive geochemical features. Abbreviations as in Fig. 2 - 4

towthe progressive decrease of fO_2 during magma evolution (e.g., Haggerty 1991). In the case of V, its concentration in magnetite is mainly in the form V^{3+} and, to a lesser extent, V^{4+} (Toplis and Carroll 1995; Bordage et al. 2011). Vanadium content in magnetite seems to correlate with temperature (e.g., Dare et al. 2014; Milani et al. 2017). Oxygen fugacity also plays a relevant role in V partitioning between magnetite and silicate melt, and a peak of V

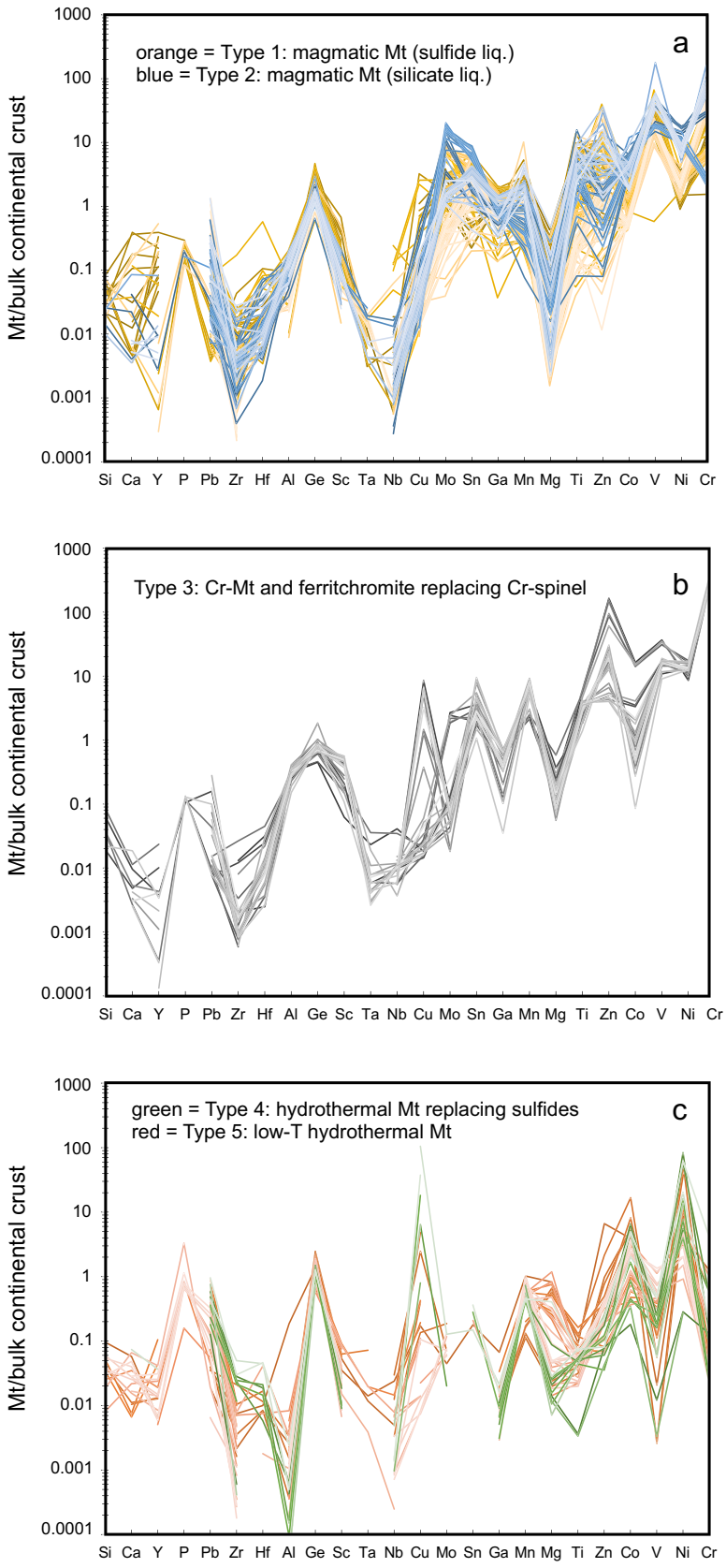

Fig. 7 Bulk continental crust-normalized, multi-element patterns for the five magnetite types (Type 1 and Type 2 in a, Type 3 in b, Type 4 and Type 5 in c). Compositions were determined via LA-ICP-MS. The order of elements is according to increasing compatibility with magnetite in silicate systems (Dare et al. 2014). Normalization factors are from Rudnick and Gao (2003)

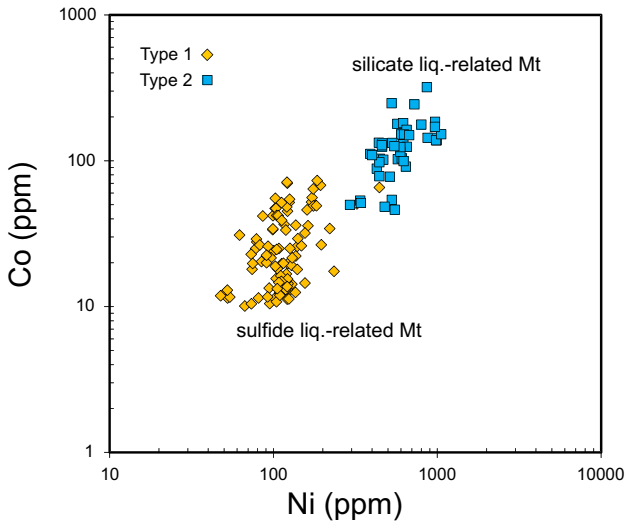

Fig. 8 Binary plot of Ni vs. Co, discriminating between magnetite segregated from sulfide (Type 1) and silicate (Type 2) liquids

in magnetite is reached at the nickel-nickel-oxide (NNO) buffer (Leeman et al. 1978; Toplis and Corgne 2002). In Fig. 10b, a partial overlap exists for Ti between magmatic and hydrothermal magnetite, which suggests that the lower-T processes were not necessarily affected by a decrease in fO_2. As for V, it discriminates between magmatic (1000–10000 ppm) and hydrothermal (< 200 ppm) magnetite. The same distinction is visible in the Ti + V vs Al + Mn diagram in Fig. 10c (Nadoll et al. 2014), where the MSS field of Noril'sk-Talnakh district is also reported for comparison purposes (Duran et al. 2020).

As mentioned, the two types of hydrothermal magnetite (Types 4 and 5) have been defined on the basis of their peculiar textural characteristics (replacement texture and stockwork microveinlets), and correspond to different mechanisms, although both are related to hydrothermal events, i.e., progressive replacement of sulfides (Type 4) and deposition of late-stage, low-T magnetite from Fe-rich fluid circulation (Type 5). A comparison between the two types in Fig. 7c shows relative enrichment in Cu, Ni, and Cr in Type 4 magnetite. It is known that copper does not readily partition into magnetite, and therefore the high Cu content (which can be > 4000 ppm) in Type 4 magnetite testifies to unavoidable incorporation of Cu minerals in the ablated material during LA-ICP-MS analysis. Type 5 magnetite is enriched in both Si and Mg compared to Type 4 magnetite (Fig. 7c and ESM4), which may suggest the incorporation of silicates (the host material in this case) in the ablated material. The representative time-signal diagrams in Fig. 11 confirm the involvement in some of the analyses of microinclusions of Cu–Zn sulfides, sometimes Pd-bearing, and silicates.

A different composition of the fluids responsible for the two types is probably the reason for the overall depletion of Zr, Ni, Cr, and Cu in Type 5 magnetite compared to Type 4 magnetite (Fig. 7c).

Magnetite as a vector to Ni-Cu mineralization in the Kunene region

The geochemistry of the magmatic sulfide-related magnetite (Type 1) indicates that, after the separation of a sulfide liquid from a silicate magma, the fractionation of sulfides

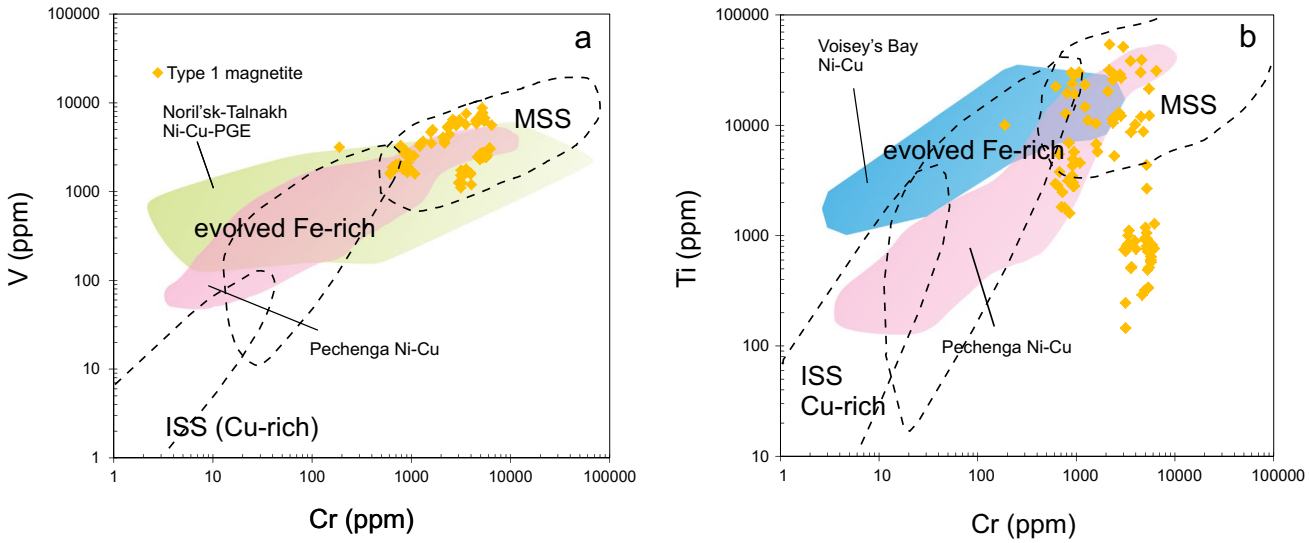

Fig. 9 (**a**) Cr vs. V and (**b**) Cr vs. Ti plotted with dashed fields representing trends of sulfide fractionation at Sudbury (data from Dare et al. 2012). Magnetite associated with MSS from other world-class Ni-Cu deposits is also shown. Primitive and evolved Fe-rich MSS of Pechenga from Moilanen et al. (2020); Noril'sk-Talnakh MSS data from Duran et al. (2020); Fe-rich MSS of Voisey's Bay (Ovoid deposit) from Boutroy et al. (2014)

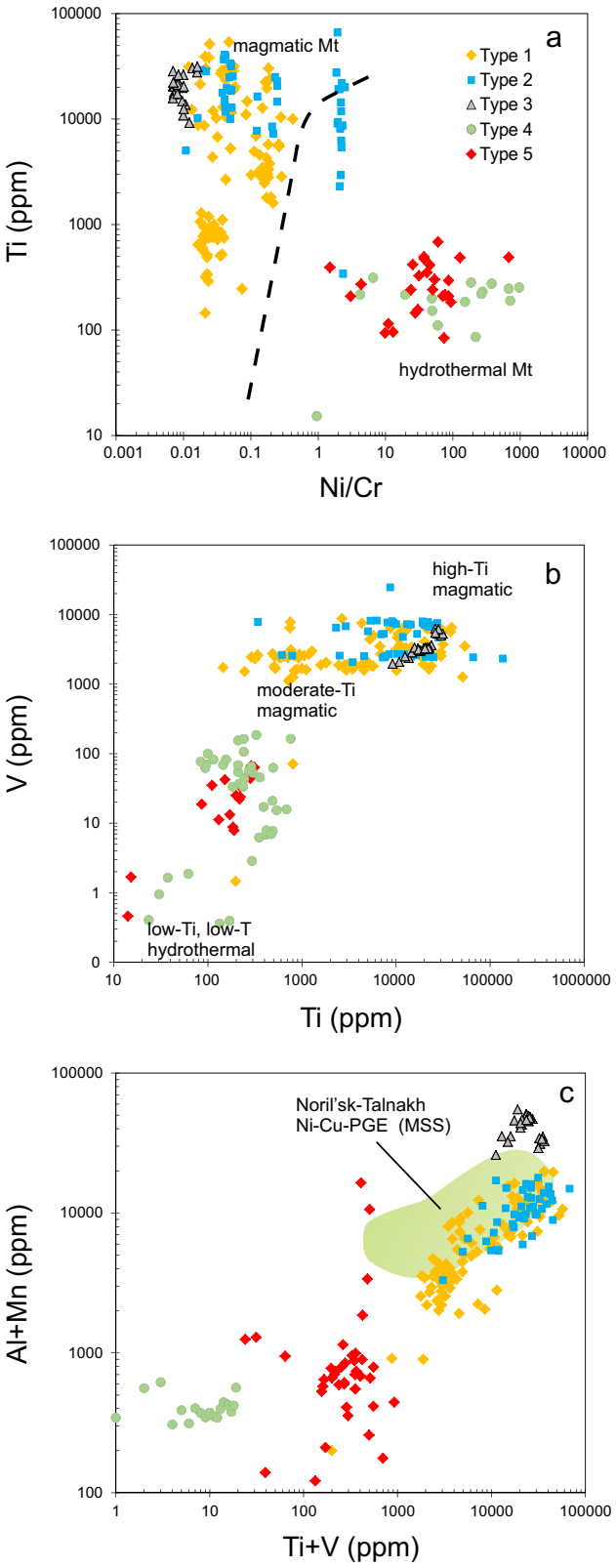

Fig. 10 Binary diagrams discriminating primary magmatic from secondary hydrothermal magnetite. **a**) Ni/Cr vs. Ti, dashed line after Dare et al. (2014); **b**) Ti vs. V; c) Al + Mn vs. Ti + V, with MSS Noril'sk-Talnakh data from Duran et al. (2020)

(mostly pyrrhotite but also pentlandite and chalcopyrite) occurred at the MSS stage. The presence of ISS-related mineralization was not detected, suggesting that this stage may have occurred when the residual sulfide liquid had migrated and was trapped elsewhere.

The seven intrusions have been relatively well investigated by exploration companies, with more than 60 cores drilled and over 3000 whole-rock geochemical assays with a range of elements (including Pt and Pd). Preliminary assessments suggest that the highest tenors in Ni-Cu, as well as PGE anomalies, are in the highly altered (serpentinized) ultramafic rocks, in particular at Ombuku North (van Zyl 2022). This suggests that post-magmatic serpentinization related to circulating hydrothermal fluids triggered sulfide remobilization and the preferential reconcentration of Ni-Cu-PGE metals. Intense serpentinization of olivine (and pyroxene) is an unequivocal indication of a low-temperature silicate alteration process induced by fluid–rock interaction, and iddingsite is indicative of alteration under oxidising conditions (Kendrick and Jamieson 2016). Hydrothermal fluid circulation can easily alter magmatic sulfides, leading to the development of secondary S-rich phases. If the fO_2 increases, a correspondingly low fS_2 in the aqueous fluids will lead to progressive desulphurization and the replacement of sulfide by magnetite, with iron released mostly by olivine and pyroxene during serpentinization (e.g., Li et al. 2004; Klein et al. 2014; Konnunaho et al. 2013; Beinlich et al. 2020). The presence of abundant magnetite replacing sulfides, in association with extensive serpentinization, is therefore an unequivocal indication of fluid circulation and, potentially, metal reconcentration. The temperature range for the formation of this type of magnetite is between 150 °C and 550 °C (Murata et al. 2009), and this replacement process was documented in many magmatic sulfide ore deposits, including Noril'sk-Talnakh (Duran et al. 2017, 2020), Lac des Îles (Duran et al. 2015), the Bushveld Complex (Li et al. 2004; Kawohl and Frimmel 2016; Kinnaird et al. 2017; Klemd et al. 2017) and the Great Dyke (Piña et al. 2016).

The mobility of PGE under post-magmatic, hydrothermal conditions, can lead to a marked upgrading of metal tenors (Mogessie et al. 1991, 2000; Pan and Wood 1994; Gál et al. 2013; Benkò et al. 2015; Holwell et al. 2017; McCreesh et al. 2018; Beinlich et al. 2020). It has also been shown that PGE (and Au) can be transferred as bisulfide (acidic-neutral/reducing to oxidising conditions) or chloride (acidic/oxidising conditions) complexes (Sassani and Shock 1990, 1998; Gammons et al. 1992; Boudreau 1993; Pan and Wood 1994; Seward and Barnes 1997; Barnes and Liu 2012; Liu et al. 2016; Sullivan et al. 2022a, b). Besides pH, the oxidation state and fluid salinity also impact the solubility of Pt and Pd (e.g., Barnes and Liu 2012). Experimental data show that

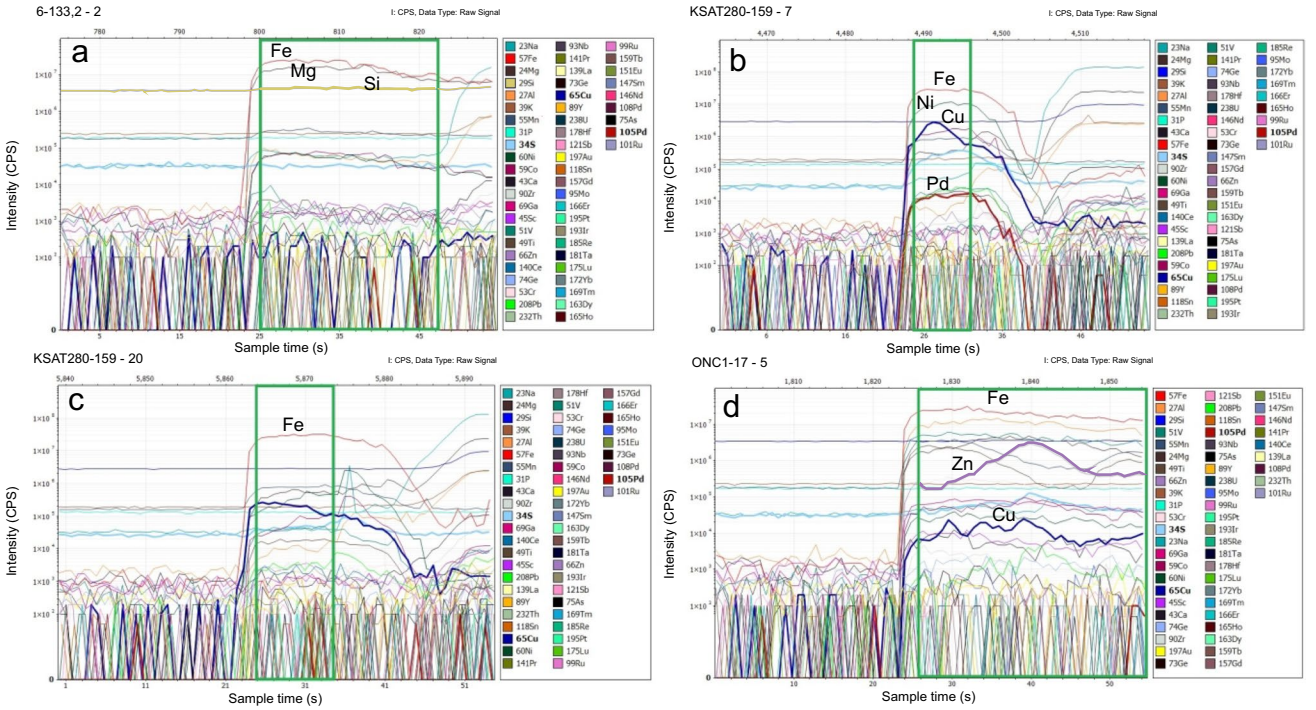

Fig. 11 Time-ablation signals for magnetite samples with anomalous signal (a, b, d) due to the presence of microinclusions or the laser partially ablating another mineral. **a**: silicate involvement in Ombuku North sample 6–133,2: **b**) microinclusion of Ni-Cu-Pd sulfide in Ombuku North sample KSAT280-159; **c**) clean magnetite signal in Ombuku North sample KSAT280-159; **d**) involvement of Cu–Zn sulfide inclusions in Oncocua sample Onc1-17. Note the high Si background in b, c, d

Pt–Pd complexes can form at temperatures as low as 300 °C (Gammons et al. 1992; Barnes and Liu 2012; Liu et al. 2016, and references therein).

The trace elements in magnetite can be used to further assess possible late-stage PGE enrichment of some of the serpentinized parts of mafic–ultramafic intrusions surrounding the Kunene Complex. Type 4 magnetite is present mostly in serpentinized ultramafic rocks, and, in this study, in serpentinized dunite (KSAT280-159) at Ombuku North and in serpentinized harzburgite (KSAT280-140) at Onyokohe. The geochemistry of Type 4 magnetite shows relative depletion in the lithophile elements Ti (15–314 ppm), Cr (b.d.l. –560 ppm), V (0.5–67 ppm), Al (b.d.l. –202 ppm), Mg (202–2486 ppm, with one outlier at 1.1 wt%), Mn (328–582 ppm) and Ga (0.05–0.34 ppm). Among the chalcophile elements, Zn (mostly < 10 ppm) is depleted, whereas those that are enriched include Ni (up to 4916 ppm), Co (up to 173 ppm) and Cu (up to 2841 ppm) (see ESM4). Magnetite analyses with Ni up to 5000 ppm and Cu up to 3000 ppm are commonly reported in literature (e.g., Dare et al. 2012; Boutroy et al. 2014; Nadoll et al. 2014; Jiao et al. 2019; Duran et al. 2020; La Cruz et al. 2020; Moilanen et al. 2020; Frank et al. 2022), and suggest minor ablation of sulfide phases present as microinclusions. For Type 4, partial contamination by sulfides is compatible with the nature of this type of magnetite as it formed by the replacement of sulfide. High base metal tenors have been observed in serpentinized ultramafic rocks in some of these intrusions (van Zyl 2022), and the association of Type 4 with these altered rocks reinforces the role of this magnetite as an indicator of mineralization.

Moreover, the frequent anomalous contents of As (max 0.89 ppm), Sb (max 8.80 ppm), and Pd (max 34.6 ppm) in Type 4 magnetite are intriguing. No arsenides and antimonides have previously been documented in these rocks, and in most of the other magnetite types, Pd is below the detection limit (max. 0.74 ppm in Type 1 magnetite, Ohamaremba troctolite KSAT280-152).

An investigation using scanning electron microscopy (SEM) and energy dispersive x-ray spectroscopy (EDS) was performed on some of the thin sections where high Pt and Pd had been found in whole-rock analyses. In various thin sections of serpentinite from Ombuku North (including KSAT280-159), micron-scale PGE minerals (antimonides, tellurides, bismuthinides, arsenides) were observed as 5–50 micron-size anhedral flakes in contact with serpentine (sperrilyte $PtAs_2$ in Fig. 4l), or associated with Type 4 magnetite as microinclusions (sperrylite, stibiopalladinite Pd_5Sb_2, moncheite $PtPd(TeBi)_2$ in Fig. 4m-o). No Pt anomalies were detected in the magnetite grains in sample KSAT280-159 from Ombuku North, but several grains show appreciable Pd, and the whole-rock assay data confirm the presence of

both Pt and Pd (273 and 301 ppb, respectively) in the serpentinized dunites of this intrusion (van Zyl 2022). A preferential enrichment in Pd over Pt in magnetite could be tentatively explained by the presence of Sb, which is a Pd carrier in post-magmatic oxidising fluids as a hydroxide complex ($Sb(OH)_3$) (Zotov et al. 2003; Obolensky et al. 2007). The diffuse alteration, combined with the high contents of As, Sb, and Pd in magnetite, and with the presence of PGE minerals as inclusions in magnetite, suggest that oxidized desulphurising fluids favoured the remobilization of primary PGE in these rocks during serpentinization. These findings, supported by the preliminary SEM study of PGE minerals in these intrusions, suggest that the primary source for PGE was magmatic sulfides, with a possible minor contribution from Cr-spinel during its alteration to ferritchromite (or Cr-magnetite).

Conclusions

Magnetite geochemistry from seven Ni-Cu-sulfide-mineralized mafic/ultramafic intrusions peripheral to the Kunene Complex has been analyzed via EPMA and LA-ICP-MS. Petrographic observations and geochemistry allow the identification of five generations of magnetite: two magmatic types, fractionated from silicate and sulfide liquids, a Cr-rich magnetite product of high-T replacement of Cr-spinel (or chromite), and two hydrothermal types: as sulfide replacement, and as late-stage, low-T disseminations and veinlets.

The classification based on textural features and mineral associations is supported by the trace element geochemistry, where the two in-situ analytical methods are complementary. Nickel and Co contents help to discriminate between the magmatic types. The magnetite geochemistry also documents the evolution of the sulfide system: elements like Cr, Co and V, whose content varies during fractionation of the sulfide liquid, suggest that most of the sulfide-related magnetite crystallized from a relatively primitive Fe-rich monosulfide solid solution (MSS). Hydrothermal processes crystallized two morphological varieties of secondary magnetite. Low trace element contents, in particular of Ni, Cr, Ti, V, Al and Mn, characterise these grains and also help to discriminate between the two hydrothermal types.

Magnetite replacing sulfides is common in serpentinized ultramafic rocks, as in Ombuku North, and is characterized by high Ni, Co, As, Sb, and, occasionally, anomalous Cu and Pd. Since Fe-oxides should have lower Cu-Pd partition coefficients than the co-existing sulfides, this suggests that these cations are present in magnetite as submicroscopic inclusions. This has been confirmed by the identification of micron-size PGE minerals as antimonides, bismuthinides, arsenides and tellurides using a scanning electron microscope.

The Ni-Cu-PGE endowment in altered (serpentinized) ultramafic rocks, the widespread desulphurization of pyrrhotite and pentlandite to magnetite rich in Pd microinclusions, and the identification of micron-sized PGE minerals associated with magnetite and serpentine, suggest metal remobilization and enrichment due to hydrothermal fluid circulation at $T \leq 300$ °C. The results of this study indicate the serpentinized ultramafic rocks as a possible target for Ni-Cu-(PGE) mineralization. This could apply to the entire system of intrusions peripheral to the KC, irrespective of the age, and can be seen as a potential condition to verify when exploring mafic/ultramafic intrusions for base metals + PGE sulfides.

Supplementary Information The online version contains supplementary material available at https://doi.org/10.1007/s00126-024-01288-x.

Acknowledgements The authors are grateful to Deon van der Mescht and Heinrich Schultz (African Nickel Limited), and to Mikhail Naumov for providing part of the samples of this work. Christian Reinke (University of Johannesburg) and Riana Rossouw (University of Stellenbosch) are thanked for assisting during the acquisition of the EPMA and LA-ICP-MS data. Natasha Ntuli (University of Pretoria) provided an important contribution through the identification of the PGE at the SEM during her Honours studies. Wolfgang Maier, Eduardo Mansur, Anne-Aurélie Sappin and an anonymous reviewer greatly improved this manuscript, and their contribution is highly appreciated. Thanks are also extended to the patience in handling the manuscript shown by the Editor-in-Chief Karen Kelley. This work has been sponsored by Anglo American as an MSc bursary to LO and was partly supported by the DSI-NRF Centre of Excellence for Integrated Mineral and Energy Resource Analysis (DSI-NRF CIMERA).

Author contribution Lorenzo Milani: Conceptualization, Writing-Original draft preparation Methodology, Investigation; Data curation.
Lize Oosthuizen: Investigation; Data curation.
Trishya M. Owen-Smith: Conceptualization, Writing, Reviewing and Editing, Supervision.
Grant M. Bybee: Conceptualization, Reviewing and Editing.
Ben Hayes: Conceptualization, Reviewing and Editing.
Jérémie Lehmann: Conceptualization, Reviewing and Editing.
Hielke Jelsma: Methodology, Resources, Validation, Reviewing and Editing.

Funding Open access funding provided by University of Pretoria.

Declarations

Competing interests This work was supported by Anglo American as an MSc grant to LO. The authors have no other competing interests to declare that are relevant to the content of this article.

References

Ahmed AH, Surour AA (2016) Fluid-related modifications of Cr-spinel and olivine from ophiolitic peridotites by contact metamorphism of granitic intrusions in the Ablah area, Saudi Arabia. J Asian Earth Sci 533:58–79. https://doi.org/10.1016/j.jseaes.2016.03.010

Ashwal LD, Twist D (1994) The Kunene complex, Angola/Namibia: a composite massif-type anorthosite complex. Geol Mag 131:579–591

Barnes SJ (2000) Chromite in komatiites, II. Modification during greenschist to mid-amphibolite facies metamorphism. J Petrol 41:387–409. https://doi.org/10.1093/petrology/41.3.387

Barnes SJ (2023) Lithogeochemistry in exploration for intrusion-hosted magmatic Ni-Cu-Co deposits. Geochemistry: Exploration Environment Analysis 23(1):17. https://doi.org/10.1144/geochem2022-025

Barnes SJ, Cruden AR, Arndt NT, Saumur BM (2016) The mineral system approach applied to magmatic Ni-Cu-PGE sulphide deposits. Ore Geol Rev 76:296–316. https://doi.org/10.1016/j.oregeorev.2015.06.012

Barnes SJ, Liu W (2012) Pt and Pd mobility in hydrothermal fluids: evidence from komatiites and from thermodynamic modelling. Ore Geol Rev 44:49–58

Barnes SJ, Roeder PL (2001) The range of spinel compositions in terrestrial mafic and ultramafic rocks. J Petrol 42:2279–2302. https://doi.org/10.1093/petrology/42.12.2279

Barra F, Gervilla F, Hernández E, Reich M, Padrón-Navarta JA, González-Jiménez JM (2014) Alteration patterns of chromian spinels from La Cabaña peridotite, south-central Chile. Mineral Petrol 108:819–836. https://doi.org/10.1007/s00710-014-0335-5

Beinlich A, von Heydebrand A, Klemd R, Martin L, Hicks J (2020) Desulphurisation, chromite alteration, and bulk rock PGE redistribution in massive chromitite due to hydrothermal overprint of the Panton Intrusion, east Kimberley, Western Australia. Ore Geol Rev 118:103288

Benkó Z, Mogessie A, Molnár F, Krenna K, Poulson RS, Hauck S, Severson M, Arehart GB (2015) Hydrothermal alteration and Cu–Ni–PGE mobilization in the charnockitic rocks of the footwall of the South Kawishiwi intrusion, Duluth Complex, USA. Ore Geol Rev 67:170–188

Blanchard JA, Ernst RE, Samson C (2017) Gravity and magnetic modelling of layered mafic–ultramafic intrusions in large igneous province plume centre regions: case studies from the 1.27 Ga Mackenzie, 1.38 Ga Kunene-Kibaran, 0.06 Ga Deccan, and 0.13–0.08 Ga High Arctic events. Can J Earth Sci 54:290–310

Bordage A, Balan E, de Villiers JR, Cromarty R, Juhin A, Carvallo C, Calasa G, Sunder Raju PV, Glatzel P (2011) V oxidation state in Fe- Ti oxides by high-energy resolution fluorescence-detected X-ray absorption spectroscopy. Phys Chem Min 38:449–458

Boudreau AE (1993) Chlorine as an exploration guide for the platinum-group elements in layered intrusions. J Geochem Explor 48:21–37

Boutroy E, Dare SAS, Beaudoin G, Barnes S-J, Lightfoot PC (2014) Magnetite composition in Ni-Cu-PGE worldwide: Application to mineral exploration. J Geochem Explor 145:64–81

Boynton WV (1985) Cosmochemistry of the rare earth elements: meteorite studies. In: Henderson P (ed) Rare earth element geochemistry, Developments in Geochemistry, vol 2. Elsevier, Amsterdam, pp 115–152

Brandt S, Klemd R, Xie H, Bobek P (2021) Unravelling the P-T-t history of three high-grade metamorphic events in the Epupa Complex, NW Namibia: implications for the Paleoproterozoic to Mesopreterozoic evolution of the Congo Craton. Amer J Sci 321:235–296

Brower AM (2017) Understanding magmatic timescales and magma dynamics in proterozoic anorthosites: a geochronological and remote sensing investigation of the kunene complex (Angola). MSc Dissertation p 86. University of Witwatersrand, Johannesburg, South Africa, p 56

Bybee GM, Hayes B, Owen-Smith TM, Lehmann J, Brower AM, Ashwal LD, Hill CM, Corfu F, Manga M (2019) Proterozoic massif-type anorthosites as the archetypes of long-lived magmatic systems: new evidence from the Kunene Anorthosite Complex (Angola). Precambr Res 332(15):105393

Dare SAS, Barnes S-J, Beaudoin G (2012) Variation in trace element content of magnetite crystallized from a fractionating sulfide liquid, Sudbury, Canada: implications for provenance discrimination. Geochim Cosmochim Acta 88:27–50. https://doi.org/10.1016/j.gca.2012.04.032

Dare SAS, Barnes S-J, Beaudoin G, Méric J, Boutroy E, Potvin-Doucet C (2014) Trace elements in magnetite as petrogenetic indicators. Miner Deposita 49:785–796

de Carvalho H, Alves P (1993) The Precambrian of SW Angola and NW Namibia. Communicações Instituto de Investigação Cientifica Trop série de ciencias da terre 4:1–38

Drüppel K, Littmann S, Romer RL, Okrusch M (2007) Petrology and isotope geochemistry of the Mesoproterozoic anorthosite and related rocks of the Kunene Intrusive Complex, NW Namibia. Precambr Res 156:1–31

Dupuis C, Beaudoin G (2011) Discriminant diagrams for iron-oxide trace element fingerprinting of mineral deposit types. Miner Deposita 46:319–335

Duran CJ, Barnes S-J, Corkery JT (2015) Chalcophile and platinum group element distribution in pyrites from the sulfide-rich pods of the Lac des Iles Pd deposits, Western Ontario, Canada: Implications for post-cumulus re-equilibration of the ore and the use of pyrite compositions in exploration. J Geochem Explor 158:223–242

Duran CJ, Barnes S-J, Corkery JT (2016a) Trace element distribution in primary sulfides and Fe–Ti oxides from the sulfide-rich pods of the Lac des Iles Pd deposits, Western Ontario, Canada: constraints on processes controlling the composition of the ore and the use of pentlandite compositions in exploration. J Geochem Explor 166:45–63. https://doi.org/10.1016/j.gexplo.2016.04.005

Duran CJ, Barnes S-J, Corkery JT (2016b) Geology, petrography, geochemistry, and genesis of sulfide-rich pods in the Lac des Iles palladium deposits, vol 51. Western Ontario, Canada: Miner Deposita, p 509–532

Duran CJ, Barnes S-J, Pleše P, Prašek MK, Zientek ML, Pagé P (2017) Fractional crystallization-induced variations in sulfides from the Noril'sk-Talnakh mining district (polar Siberia, Russia). Ore Geol Rev 90:326–351

Duran CJ, Barnes S-J, Mansur ET, Dare SAS, Bedard LP, Sluzhenikin SF (2020) Magnetite chemistry by laser ablation-inductively coupled plasma-mass spectrometry records sulfide fractional crystallization in massive nickel-copper-platinum group element ores from the Norilsk-Talnakh Mining District (Siberia, Russia): implications for trace element partitioning into magnetite. Econ Geol 115:1245–1265

Ernst RE, Pereira E, Hamilton MA, Pisarevsky SA, Rodriques J, Tassinari CCG, Teixeira W, Van-Dunem V (2013) Mesoproterozoic intraplate magmatic 'barcode' record of the Angola portion of the Congo craton: newly dated magmatic events at 1500 and

1110 Ma and implications for Nuna (Columbia) supercontinent reconstructions. Precambr Res 230:103–118
Evans BW (2008) Control of the products of serpentinization by the Fe^{2+} Mg^{-1} exchange potential of olivine and orthopyroxene. J Petrol 49:1873–1887
Evans DAD (2013) Reconstructing pre-Pangean supercontinents. Geol Soc Am Bull 125:1735–1751
Ferreira E, Lehmann J. Rodrigues JF, Hayes B, Merino-Martinez E, Milani L, Bybee GM, Owen-Smith TM, García-Lobón JL, Tassinari CCG, Ueckermann H, Sato K, Silva PB, Correia J, Labaredas J, Duarte L, Molekwa MA, Manuel J, da Mata A, Victorino L (2024) Zircon U-Pb and Lu-Hf isotopes reveal the crustal evolution of the SW Angolan Shield (Congo Craton). Gondwana Res 131: 317-342
Fonseca ROC, Campbell AH, O'Neill HSC, Fitzgerald JD (2008) Oxygen solubility and speciation in sulphide-rich mattes. Geochim Cosmochim Acta 72:2619–2635
Frank KS, Spry PG, O'Brien JJ, Koenig A, Allen RL, Jansson N (2022) Magnetite as a provenance and exploration tool for metamorphosed base-metal sulfide deposits in the Stollberg ore field, Bergslagen, Sweden. Min Mag 86:373–396
Frost KM, Groves DI (1989) Magmatic contacts between immiscible sulfide and komatiite melts: implications for the genesis of Kambalda sulfide ores. Econ Geol 84:697–1704. https://doi.org/10.2113/gsecongeo.84.6.1697
Gaetani GA, Grove TL (1997) Partitioning of moderately siderophile elements among olivine, silicate melt, and sulfide melt: Constraints on core formation in the Earth and Mars. Geochim Cosmochim Acta 61:1829–1846
Gál B, Molnár F, Guzmics T, Mogessie A, Szabó C, Peterson DM (2013) Segregation of magmatic fluids and their potential in the mobilization of platinum-group elementsin the South intrusion, Duluth Complex, Minnesota — evidence from petrography, apatite geochemistry and coexisting fluid and melt inclusions. Ore Geol Rev 54:59–80
Gammons CH, Bloom MS, Yu Y (1992) Experimental investigation of the hydrothermal geochemistry of platinum and palladium: I. Solubility of platinum and palladium sulphide minerals in $NaCl/H_2SO_4$ solutions at 3008C. Geochim Cosmochim Acta 56:3881–3894
González-Jiménez JM, Kerestedjian T, Fernández JAP, Linares FG (2009) Metamorphism on chromite ores from the Dobromirtsi Ultramafic Massif, Rhodope Mountains (SE Bulgaria). Geol Acta 7:413–429
Haggerty SE (1991) Oxide textures: a mini-atlas. Mineral Soc Am Rev Mineral 25:129–219
Hirschmann MM, Ghiorso MS (1994) Activities of nickel, cobalt, and manganese silicates in magmatic liquids and applications to olivine/liquid and to silicate/metal partitioning. Geochim Cosmochim Acta 58:4109–4126
Hodel F, Macouin M, Triantafyllou A, Carlut J, Berger J, Rousse S, Ennih N, Trindade RIF (2017) Unusual massive magnetite veins and highly altered Cr-spinels as relics of a Cl-rich acidic hydrothermal event in Neoproterozoic serpentinites (Bou Azzer ophiolite, Anti-Atlas, Morocco). Precambr Res 300:151–167. https://doi.org/10.1016/j.precamres.2017.08.005
Hodel F, Macouin M, Trindade RIF, Araujo JFDF, Respaud M, Meunier JF, Cassayre L, Rousse S, Drigo L, Schorne-Pinto J (2020) Magnetic properties of ferritchromite and cr-magnetite and monitoring of crspinels alteration in ultramafic and mafic rocks. Geochem Geophys 21:e2020GC009227. https://doi.org/10.1029/2020GC009227
Holwell DA, Adeyemi Z, Ward LA, Smith DJ, Graham SD, McDonald I, Smith JW (2017) Low temperature alteration of magmatic Ni-Cu-PGE sulfides as a source for hydrothermal Ni and PGE ores: a quantitative approach using automated mineralogy. Ore Geol Rev 91:718–740
Hornsey R, Naumov M, Fraenkel H (2009) Ni-PGE mineralization within the Namibian Kunene Complex-evidence for a continental-scale Kibaran Ni-PGE mineralizing event [abs.]: In Proceedings of the Xi'an International Ni-Cu (Pt) deposit Symposium, China, Northwestern Geology, Xi'an, China, Abstracts 42:143–146
Huang X-W, Sappin A-A, Boutroy E, Beaudoin G, Makvandi S (2019) Trace Element Composition of Igneous and Hydrothermal Magnetite from Porphyry Deposits: Relationship to Deposit Subtypes and Magmatic Affinity. Econ Geol 114:917–952
Jiao J, Han F, Zhao L, Duan J, Wang M (2019) Magnetite Geochemistry of the Jinchuan Ni-Cu-PGE Deposit, NW China: Implication for Its Ore-Forming Processes. Minerals 9:593. https://doi.org/10.3390/min9100593
Jelsma HA, McCourt S, Perritt SH, Armstrong RA (2018) The geology and evolution of the Angolan Shield, Congo Craton. In: Siegesmund S, Basei MAS, Oyhantçabal P, Oriolo S (eds) Geology of Southwest Gondwana. Springer International Publishing, Cham, pp 217–239
Kawohl A, Frimmel HE (2016) Isoferroplatinum-pyrrhotite-troilite intergrowth as evidence of desulfurization in the Merensky Reef at Rustenburg (western Bushveld Complex, South Africa). Mineral Mag 80:1041–1053
Kegler Ph, Holzheid A, Frost DJ, Rubie DC, Dohmen R, Palme H (2008) New Ni and Co metal-silicate partitioning data and their relevance for an early terrestrial magma ocean. Earth Planet Sci Lett 268:28–40
Kendrick JL, Jamieson RA (2016) The fate of olivine in the lower crust: pseudomorphs after olivine in coronitic metagabbro from the Grenville Orogen, Ontario. Lithos 260:356–370
Kerr A, Smith J (1997) The search for magmatic Ni-Cu-Co mineralization in northern Labrador: a summary of active exploration programs. Newfoundland Department of Mines and Energy, Geological Survey Branch, Report, 97–1
Kinnaird JA, Yudovskaya M, McCreesh M, Huthmann F, Botha TJ (2017) The Waterberg Platinum Group Element Deposit: Atypical Mineralization in Mafic-Ultramafic Rocks of the Bushveld Complex, South Africa. Econ Geol 112:1367–1394
Kinzler RJ, Grove TL, Recca SI (1990) An experimental study on the effect of temperature and melt composition on the partitioning of nickel between olivine and silicate melt. Geochim Cosmochim Acta 54:1255–1265
Klein F, Bach W, Humphris SE, Kahl W-A, Jöns N, Moskowitz B, Berquó TS (2014) Magnetite in seafloor serpentinite-Some like it hot. Geology 42:135–138
Klemd R, Herderich T, Junge M, Oberthür T, Schouwstra R, Roberts J (2017) Platinum-group element concentrations in base-metal sulphides from the Platreef, Mogalakwena Platinum Mine, Bushveld Complex, South Africa. S Afr J Geol 119:623–638
Konnunaho J, Hanski EH, Bekker A, Halkoaho TAA, Hiebert RS, Wing BA (2013) The Archean komatiite-hosted, PGE-bearing Ni-Cu sulphide deposit at Vaara, eastern Finland: evidence for assimilation of external sulfur and post-depositional desulfurization. Miner Deposita 48:967–989
Kröner A, Rojas-Agramonte Y, Hegner E, Hoffmann K-H, Wingate MTD (2010) SHRIMP zircon dating and Nd isotopic systematics of Palaeoproterozoic migmatitic orthogneisses in the Epupa Metamorphic Complex of northwestern Namibia. Precambr Res 183(1):50–69
Kröner A, Rojas-Agramonte Y, Wong J, Wilde SA (2015) Zircon reconnaissance dating of Proterozoic gneisses along the Kunene River of northwestern Namibia. Tectonophysics 662:125–139

La Cruz NL, Ovalle JT, Simon AC, Konecke BA, Barra F, Reich M, Leisen M, Childress T (2020) The Geochemistry of Magnetite and Apatite from the El Laco Iron Oxide-Apatite Deposit, Chile: Implications for Ore Genesis. Econ Geol 115:1461–1491

Lee CTA, Luffi P, Chin EJ, Bouchet R, Dasgupta R, Morton DM, Le Roux V, Yin QZ, Jin D (2012) Copper systematics in arc magmas and implications for crust-mantle differentiation. Science 336:64–68

Leeman WP, Ma MS, Murali AV, Schmitt RA (1978) Empirical estimation of magnetite/liquid distribution coefficients for some transition elements. Contrib Mineral Petrol 65:269–272

Lehmann J, Bybee GM, Hayes B, Owen-Smith T, Belyanin G (2020) Emplacement of the giant Kunene AMCG complex into a contractional ductile shear zone and implications for the Mesoproterozoic tectonic evolution of SW Angola. Int J Earth Sci. https://doi.org/10.1007/s00531-020-01837-5

Li C, Naldrett A (1999) Geology and petrology of the Voisey's Bay intrusion: reaction of olivine with sulfide and silicate liquids. Lithos 47(1–2):1–31

Li C, Ripley EM (2010) The relative effects of composition and temperature on olivine-liquid Ni partitioning: Statistical deconvolution and implications for petrologic modeling. Chem Geol 275:99–104

Li C, Ripley EM, Merino E, Maier WD (2004) Replacement of base metal sulfides by actinolite, epidote, calcite, and magnetite in the UG2 and Merensky reef of the Bushveld Complex, South Africa. Econ Geol 99:173–184

Li Y, Audétat A (2012) Partitioning of V, Mn Co, Ni, Cu, Zn, As, Mo, Ag, Sn, Sb, W, Au, Pb, and Bi between sulfide phases and hydrous basanite melt at upper mantle conditions. Earth Planet Sci Lett 355–356:327–340

Lightfoot PC, Evans-Lamswood DM (2015) Structural controls on the primary distribution of mafic-ultramafic intrusions containing Ni-Cu-Co- (PGE) sulfide mineralization in the roots of large igneous provinces. Ore Geol Rev 64:354–386

Liu P-P, Zhou M-F, Chen WT, Gao J-F, Huang X-W (2015) In-situ LA-ICP-MS trace elemental analyses of magnetite: e–Ti–(V) oxide-bearing mafic–ultramafic layered intrusions of the Emeishan Large Igneous Province, SW China. Ore Geol Rev 65:853–871

Liu T, Mungall JE, Ames D (2016) Hydrothermal Redistribution and Local Enrichment of Platinum Group Elements in the Tootoo and Mequillon Magmatic Sulfide Deposits, South Raglan Trend, Cape Smith Belt, New Quebec Orogen. Economic Geology 111, 467–485.McDonald, I., Ohnenstetter, D., Rowe, J.P., Tredoux, M., Pattrick, R.A.D., Vaughan, D.J., 1999. Platinum precipitation in the Waterberg deposit, Naboomspruit, South Africa. S Afr J Geol 102:184–191

MacLean WH, Shimakazi H (1976) The Partition of Co, Ni, Cu, and Zn between Sulfide and Silicate Liquids. Econ Geol 71:1049–1057

Maier WD, Teigler B, Miller R (2008) The Kunene anorthosite complex and its satellite intrusions. The geology of Namibia. Geol Surv Namibia 9(1):9–18

Maier WD, Rasmussen B, Fletcher IR, Li C, Barnes SJ, Huhma H (2013) The Kunene anorthosite complex, Namibia, and its satellite intrusions: geochemistry, geochronology, and economic potential. Econ Geol 108(5):953–986

Mäkitie H, Data G, Isabirye E, Mäntärri I, Huhma H, Klausen MB, Pakkenen L, Virransaio P (2014) Petrology, geochronology and emplacement model of the giant 1.37 Ga arcuate Lake Victoria dyke swarm on the margin of a large igneous province in eastern Africa. J Afr Earth Sci 97:273–296

Marques AFA, Barriga FJAS, Scott SD (2007) Sulfide mineralization in an ultramafic-rock hosted seafloor hydrothermal system: From serpentinization to the formation of Cu–Zn–(Co)-rich massive sulfides. Mar Geolo 245:20–39. https://doi.org/10.1016/j.margeo.2007.05.007

Matzen AK, Baker MB, Beckett JR, Stolper EM (2013) The temperature and pressure dependence of nickel partitioning between olivine and silicate melt. J Petrol 54:2521–2545

Mayer A, Hofmann AW, Sinigoi S, Morais E (2004) Mesoproterozoic Sm-Nd and UPb ages for the Kunene anorthosite complex of SW Angola. Precambr Res 133:187–206

McCourt S, Armstrong RA, Jelsma H, Mapeo RBM (2013) New U-Pb SHRIMP ages from the Lubango region, SW Angola: insights into the Palaeoproterozoic evolution of the Angolan Shield, southern Congo Craton, Africa. J Geol Soc London 170(2):353–363

McCreesh MJG, Yudovskaya MA, Kinnaird JA, Reinke C (2018) Platinum-group minerals of the F and T zones, Waterberg Project, far northern Bushveld Complex: implication for the formation of the PGE mineralization. Mineral Mag 82:539–575

Mellini M, Rumori C, Viti C (2005) Hydrothermally reset magmatic spinels in retrograde serpentinites: Formation of "ferritchromit" rims and chlorite aureoles. Contrib Mineral Petrol 149:266–275. https://doi.org/10.1007/s00410-005-0654-y

Merlini A, Grieco G, Diella V (2009) Ferritchromite and chromian-chlorite formation in mélange-hosted Kalkan chromitite (Southern Urals, Russia). Amer Miner 94:1459–1467

Milani L, Bolhar R, Cawthorn RG, Frei D (2017) In situ LA–ICP-MS and EPMA trace element characterization of Fe–Ti oxides from the phoscorite–carbonatite association at Phalaborwa, South Africa. Miner Deposita 52:747–768. https://doi.org/10.1007/s00126-016-0696-2

Milani L, Lehmann J, Bybee GM, Hayes B, Owen-Smith TM, Oosthuizen L, Delport PWJ, Ueckermann H (2022) Geochemical and geochronological constraints on the Mesoproterozoic Red Granite Suite, Kunene AMCG Complex of Angola and Namibia. Precambr Res 379:106821

Mogessie A, Stumpfl EF, Weiblen PW (1991) The role of fluids in the formation of platinum-group minerals, Duluth Complex, Minnesota; mineralogic, textural, and chemical evidence. Econ Geol 86:1506–1518

Mogessie A, Hauzenberger Ch, Hoinkes G, Felfering A, Stumpfl EF, Bjerg EA, Kostadinoff J (2000) Genesis of platinum-group minerals in the Las Aguilas mafic-ultramafic rocks, San Luis Province, Argentina: textural, chemical and mineralogical evidence. Mineral Petrol 68:85–114

Moilanen M, Hanski E, Konnunaho J, Törmänen T, Yang S-H, Lahaye Y, O'Brien H, Illikainen J (2020) Composition of iron oxides in Archean and Paleoproterozoic mafic-ultramafic hosted Ni-Cu-PGE deposits in northern Fennoscandia: application to mineral exploration. Miner Deposita 55:1515–1534

Mudd GM, Jowitt SM (2022) The new century for nickel resources, reserves, and mining: Reassessing the sustainability of the devil's metal. Econ Geol 117(8):1961–1983

Murata K, Maekawa H, Yokose H, Yamamoto K, Fujioka K, Chiba H, Ishii T, Wada Y (2009) Significance of serpentinization of wedge mantle peridotites beneath Mariana forearc, western Pacific: Geosphere 5:90–104

Mysen BO (1978) Experimental determination of nickel partition coefficients between liquid, pargasite, and garnet peridotite minerals and concentration limits of behavior according to Henry's law at high pressure and temperature. Amer J Sci 278:217–243

Mysen BO, Kushiro I (1979) Pressure dependence of nickel partitioning between forsterite and aluminous silicate melts. Earth Planet Sci Lett 42:383–388

Nadoll P, Angerer T, Mauk JL, French D, Walshe J (2014) The chemistry of hydrothermal magnetite: a review. Ore Geol Rev 61:1–32

Naldrett AJ (1997) Key factors in the genesis of Noril'sk, Sudbury, Jinchuan, Voisey's Bay and other world-class Ni-Cu-PGE deposits: Implications for exploration. Aus J Earth Sci 44(3):283–315
Naldrett AJ (2004) Magmatic sulfide deposits. Geology, Geochemistry and Exploration. Springer, Berlin, p 728
Naumov MV (2008) Geology of the Ombuku North, Ombuku South and Ohamaremba local areas (Kunene region, northern Namibia). Anglo American unpublished internal report, p 53
Obolensky AA, Gushchina LV, Borisenko AS, Borovikov AA, Pavlova GG (2007) Antimony in hydrothermal processes: solubility, conditions of transfer, and metal-bearing capacity of solution. Russian Geol Geoph 48:992–1001
Pan P, Wood SA (1994) Solubility of Pt and Pd sulfides and Au metal in aqueous bisulfide solutions; II, results at 2008C to350 8C and saturated vapor pressure. Miner Deposita 29:373–390
Pereira E, Tassinari CG, Rodrigues JF, Van-Dúnen MV (2011) New data on the deposition age of the volcano-sedimentary Chela Group and its Eburnean basement: implications to post-Eburnean crustal evolution of the SW of Angola. Comunicações Geológicas Do LNEG 9:27–40
Piña R, Gervilla F, Barnes S-J, Oberthür T, Lunar R (2016) Platinum-group element concentrations in pyrite from the Main sulfide zone of the Great Dyke of Zimbabwe. Miner Deposita 51:853–852
Pisiak LK, Canil D, Lacourse T, Plouffe A, Ferbey T (2017) Magnetite as an indicator mineral in the exploration of porphyry deposits: a case study in till near the Mount Polley Cu-Au deposit, British Columbia, Canada. Econ Geol 112:919–940
Rey-Moral C, Mochales T, Merino Martínez E, García Lobón JL, López Bahut MT, Martín-Banda R, Feria MC, Ballesteros D, Machadinho A, Alves D (2022) Recording the largest gabbro-anorthositic complex worldwide: The Kunene Complex (KC), SW Angola. Precambr Res 379:106790
Rudnick RL, Gao S (2003) Composition of the continental crust. In Holland HD, Turekian KK (eds). Treatise on geochemistry p 1–64. Elsevier-Pergamon, Oxford
Ryan B (2000) The Nain-Churchill boundary and the Nain Plutonic Suite: A regional perspective on the geologic setting of the Voisey's Bay Ni-Cu-Co deposit. Econ Geol 95(4):703–724
Ryan B, Wardle RJ, Gower CF, Nunn GAG (1995) Nickel–copper sulfide mineralization in Labrador: the Voisey Bay discovery and its exploration implications. In: Geological Survey, Department of Natural Resources, Government of Newfoundland and Labrador Current Research Report 95:177–204
Sassani DC, Shock EL (1990) Speciation and solubility of palladium in aqueous magmatic-hydrothermal solutions. Geology 18:925–928
Sassani DC, Shock EL (1998) Solubility and transport of platinum-group elements in supercritical fluids: summary and estimates of thermodynamic properties for ruthenium, rhodium, palladium, and platinum solids, aqueous ions, and complexes to 1000 °C and 5 kbar. Geochim Cosmochim Acta 62:2643–2671
Saumur BM, Hattori K (2013) Zoned Cr-spinel and ferritchromite alteration in forearc mantle serpentinites of the Rio San Juan Complex, Dominican Republic. Mineral Mag 77(1):117–136
Scoates JS, Mitchell JN (2000) The evolution of troctolitic and high Al basaltic magmas in Proterozoic anorthosite plutonic suites and implications for the Voisey's Bay massive Ni-Cu sulfide deposit. Econ Geol 95(4):677–701
Selfe GR (2009) New discovery of Ni mineralization in Northern Namibia—geophysical case study [abs.]: SAGA Biennial Technical Meeting and Exhibition, 11th, Swaziland, Abstracts: 33–38
Seth B, Armstrong RA, Brandt S, Villa IM, Kramers JD (2003) Mesoproterozoic U-Pb and Pb–Pb ages of granulites in NW Namibia: reconstructing a completeorogenic cycle. Precambr Res 126(1–2):147–168
Seth B, Armstrong RA, Büttner A, Villa IM (2005) Time constraints for Mesoproterozoic upper amphibolite facies metamorphism in NW Namibia: a multiisotopic approach. Earth Planet Sci Lett 230(3–4):355–378
Seward TM, Barnes HL (1997) Metal transport by hydrothermal ore fluids. In: Barnes HL (ed) Geochemistry of hydrothermal ore deposits, 3rd edn. Wiley, New York, pp 435–486
Simpson ESW, Clifford TN, Gass IG (1970) The anorthosite of southern Angola: A review of present data. African magmatism and tectonics: Edinburgh, Oliver and Boyd, p 461
Sobolev AV, Hofmann AW, Sobolev SV, Nikogosian IK (2005) An olivine-free mantle source of Hawaiian shield basalts. Nature 434:590–597
Sullivan NA, Zajacz Z, Brenan JM, Hinde JC, Tsay A, Yin Y (2022) The solubility of gold and palladium in magmatic brines: Implications for PGE enrichment in mafic-ultramafic and porphyry environments. Geochim Cosmochim Acta 316:230–252
Sullivan NA, Zajac Z, Brenan JM, Tsay A (2022b) The solubility of platinum in magmatic brines: Insights into the mobility of PGE in ore-forming environments. Geochim Cosmochim Acta 316:253–272
Tack L, Wingate MTD, De Waele B, Meert J, Belousova E, Griffin B, Tahon A, Fernandez-Alonso M (2010) The 1375 Ma "Kibaran event" in central Africa: Prominent emplacement of bimodal magmatism under extensional regime. Precambr Res 180:63–84
Toplis MJ, Carroll MR (1995) An experimental study of the influence of oxygen fugacity on Fe–Ti oxide stability, phase relations, and mineral– melt equilibria in ferro-basaltic systems. J Petrol 36:1137–1170
Toplis MJ, Corgne A (2002) An experimental study of element partitioning between magnetite, clinopyroxene and iron-bearing silicate liquids with particular emphasis on vanadium. Contrib Mineral Petrol 144:22–37
van Zyl AC (2022) Geochemistry and geochronology of the peripheral intrusions to the Kunene Anorthosite Complex in southern Angola and northern Namibia, University of Pretoria, MSc Dissertation, p 107
Ward LA, Holwell DA, Barry TL, Blanks DE, Graham SD (2018) The use of magnetite as a geochemical indicator in the exploration for magmatic Ni-Cu-PGE sulfide deposits: a case study from Munali, Zambia. J Geochem Explor 188:172–184. https://doi.org/10.1016/j.gexplo.2018.01.018
Yang S-H, Yang G, Qu W, Du A, Hanski E, Lahaye Y, Chen J (2018) Pt-Os isotopic constraints on the age of hydrothermal overprinting on the Jinchuan Ni-Cu-PGE deposit, China. Miner Deposita 53:757–774
Zhao WW, Zhou M-F (2015) In-situ LA–ICP-MS trace elemental analyses of magnetite: The Mesozoic Tengtie skarn Fe deposit in the Nanling Range, South China. Ore Geol Rev 65:872–883
Zhou M-F, Chen WT, Wang CY, Prevec SA, Liu PP, Howarth GH (2013) Two stages of immiscible liquid separation in the formation of Panzhihua-type Fe-Ti-V oxide deposits, SW China. Geosci Frontiers 4:481–502
Zotov AV, Shikina ND, Akinfiev NN (2003) Thermodynamic properties of the Sb(III) hydroxide complex $Sb(OH)_3(aq)$ at hydrothermal condition. Geochim Cosmochim Acta 67:1821–1836